



The Piuquencillo Fault System: a long-lived, Andean-transverse fault system and its relationship with magmatic and hydrothermal activity

José Piquer¹, Orlando Rivera², Gonzalo Yáñez^{3,4,5}, Nicolás Oyarzún¹

¹Instituto de Ciencias de la Tierra, Universidad Austral de Chile, Valdivia, 5090000, Chile

5 ²Minera Peñoles de Chile, Santiago, 8320000, Chile

³Departamento de Ingeniería Estructural y Geotécnica, Pontificia Universidad Católica de Chile, Santiago, 8320000, Chile

⁴Centro de Excelencia en Geotermia de los Andes (CEGA), Santiago, 8320000, Chile

⁵Núcleo Milenio Trazadores de Metales (NMTM), Santiago, 8320000, Chile

Correspondence to: José Piquer (jose.piquer@uach.cl)

10 **Abstract.** Lithospheric-scale fault systems control the large-scale permeability in the Earth's crust and lithospheric mantle, and its proper recognition is fundamental to understand the geometry and distribution of mineral deposits, volcanic and plutonic complexes and geothermal systems. However, their manifestations at the current surface can be very subtle, as in many cases they are oriented oblique to the current continental margin and to the axis of the magmatic arc, can be partially obliterated by younger, arc-parallel faults, and can also be covered by volcanic and sedimentary deposits, through which the fault might
15 propagate vertically.

The Piuquencillo Fault System (PFS) is a proposed lithospheric-scale fault system, located in the Main Cordillera of Central Chile. Here we present the results of the first detailed field study of the PFS, based on structural data collected at 82 structural stations distributed across all the Western Main Cordillera. The first published U-Pb zircon ages for the La Obra batholith, which is bounded to the south by the PFS but it is also affected by younger reactivations of it, were obtained. They yielded
20 20.79 ± 0.13 Ma (granodiorite) and 20.69 ± 0.07 (monzogranite). Statistical analysis of fault plane data shows that the presence of the PFS is reflected on a strong preferred NW to WNW strike, with variable dip directions, evident from the analysis of the total fault plane population and also from individual segments of the PFS. In some segments, the presence of major NE to ENE-striking faults which intersect the PFS is also reflected in the preferred orientation of fault planes. Preferred orientations of hydrothermal veins, breccias and dikes show that both the PFS and some ENE-striking faults were capable of channeling
25 hydrothermal fluids and magma. Kinematic and dynamic analysis of fault-plane data reveals that most of the PFS was reactivated with sinistral \pm reverse kinematics during the Neogene, under a strike-slip to transpressive regime with E- to ENE-trending shortening direction (σ_1). Detailed kinematic and dynamic analyses were completed for various segments of the PFS and also for the different rock units affected by it.

This study supports the concept that the PFS is a lithospheric-scale fault system, which strongly controlled deformation and
30 the flow of magmas and hydrothermal fluids during the Neogene. The PFS forms part of a larger, margin-transverse structure, the Maipo Deformation Zone, a continental-scale discontinuity which cut across the entire Chilean continental margin, and which has been active at least since the Jurassic.



1 Introduction

Lithospheric-scale fault systems control the large-scale permeability of the crust and lithospheric mantle (McCuaig and Hronsky, 2014), and their proper recognition is fundamental to understand the distribution and geometry of magmatic-hydrothermal systems and the mineral deposits, volcanic complexes and geothermal systems with which they might be related. However, their manifestations in the present-day surface can be very subtle, as in many cases they are oriented oblique to the axis of younger magmatic arcs and can be obliterated by younger, arc-parallel faults and might also be covered by volcanic and sedimentary deposits through which the fault has to propagate vertically (Fig. 1).

In the Chilean and Argentinean Andes, several authors have proposed the existence of pre-Andean, lithospheric-scale structures which are oblique to the N-trending present-day continental margin (Salfity, 1985; Chernicoff et al., 2002). It has been suggested that this pre-Andean structures control the distribution of fossil and active magmatic-hydrothermal centres, including those related to porphyry deposits in northern and central Chile (Richards et al., 2001; Piquer et al., 2016) and volcanic and geothermal systems in the southern part of the country (Cembrano and Lara, 2009). This type of structures also bound uplifted basement blocks, and acted as basin-bounding faults during various episodes of extensional deformation during Andean evolution (Yáñez and Rivera, 2019). However, for most of these structures their field expression remains unclear, as they have been inferred from different types of lineaments or alignments, from geophysical data sets and from abrupt regional-scale discontinuities of N-trending geological units. Here we present the first field-based study of the Piuquencillo Fault System (PFS), a proposed lithospheric-scale structure present in the Andes of central Chile, including a characterization of its kinematics and related paleo-stress tensors, for each individual segment of the PFS. Then we complement our results with different types of geological and geophysical data, to provide an integral characterization of this fault system, and we discuss the relevance of this long-lived structure during Andean evolution up to this day, including its role as a pathway for magmas and hydrothermal fluids, and its potential seismic hazard for Chile's most densely populated area.

2 Geological background

The Main Cordillera of central Chile (Fig. 2) was the position of the Paleogene-Neogene magmatic arc. Consequently, it is composed mostly of Cenozoic volcanic and intrusive rocks, with subordinate sedimentary intercalations. The evolution of this magmatic arc is characterized by the opening and subsequent inversion of the Abanico Basin (Charrier et al., 2002), an intra-arc volcano-tectonic basin formed between the Late Eocene and the Early Miocene and inverted in specific, short-lived pulses of compressive deformation since the Early Miocene (Charrier et al., 2002; Piquer et al., 2017). The widespread volcanic and sedimentary deposits accumulated during the extensional stages of the basin have been grouped into two main stratigraphic units: the Abanico Formation (Aguirre, 1960; Thomas, 1953), in the area to the east of the city of Santiago (Fig. 2), and the Coya-Machalí Formation (Klohn, 1960) in the mountain regions to the south of it (Fig. 2). The thickness of these units is highly variable, although it can reach up to 5 km (Piquer et al., 2017).



65 Tectonic inversion since the Early Miocene was associated with a decrease in the rates of volcanic output and with the
emplacement in the upper crust of a series of Miocene to early Pliocene plutons (Fig. 2). Volcanic rocks accumulated during
tectonic inversion are grouped into the Farellones Formation in the area to the east of Santiago (Klohn, 1960), and the Teniente
Volcanic Complex (TVC) towards the south (Godoy, 1993; Kay et al., 2005; Fig. 2). The final stages of Neogene magmatism
produced large, differentiated, upper-crustal magmatic-hydrothermal complexes, which led to the formation of two giant
porphyry Cu-Mo deposits: Río Blanco-Los Bronces and El Teniente (Fig. 2). After the formation of these two mineral deposits,
70 the magmatic arc migrated ~40 km towards the east.

The NW to WNW-striking PFS was defined during regional-scale geological studies around the El Teniente Cu-Mo porphyry
deposit by Rivera and Falcon (2000). These authors indicated that the fault has an average strike of N60°W, dipping 70-80°
towards the south. It was proposed that the fault acted as a basin-bounding fault during extensional deformation related to the
opening of the Abanico Basin; the Coya-Machalí Formation, which according to the authors has a larger sedimentary
75 component than the also syn-extensional Abanico Formation, appeared to be present only to the south of the PFS. A set of
sheeted dikes was emplaced later along different branches of the PFS. Later studies, based on U-Pb zircon geochronology and
whole-rock geochemistry, confirmed that the PFS constitute a major boundary between two contrasting segments of the
Abanico Basin (Piquer et al., 2017; Fig. 2), characterized by different stratigraphic units and also showing major differences
in their tectonic evolution and exhumation history. In the northern segment, which contains the Río Blanco-Los Bronces
80 porphyry, stratigraphic units correspond to the Abanico Formation (~34-22 Ma) and the Farellones Formation (~22-16 Ma),
commonly separated by progressive unconformities. In the southern segment, the Abanico Formation is also present, but is
covered by the younger Coya-Machalí Formation (23-13 Ma), which is in turn covered by the sub-horizontal volcanic deposits
of the TVC (13-6 Ma; Piquer et al., 2017). REE patterns in igneous rocks also show major differences between the northern
and southern segments (Piquer et al., 2017); this can be observed in the depletion of HREE documented in lava flows of the
85 Farellones Fm., not observed in the coeval deposits of the Coya-Machalí Fm., and also in middle Miocene plutons emplaced
in both segments, which also show a clearly stronger depletion of HREE and steeper REE patterns in the northern segment.
This suggest that the northern segment was affected by compressive deformation and crustal thickening earlier than the
southern segment.

3 Methodology

90 Figure 3 shows the distribution of structural stations within the PFS and surrounding areas. Data was captured during three
field campaigns, between 2016 and 2018. From the 82 structural stations shown in Fig. 3, 240 fault planes were measured, 54
of them containing kinematic information. The parameters measured in each fault plane were strike and dip, rake of striation,
thickness of the fault and its damage zone, hydrothermal mineral infill (when present) and, when possible, sense of movement
based on different kinematic criteria for brittle faults (Fig. 4). Most kinematic indicators are related to the geometry of syn-
95 tectonic hydrothermal minerals (Fig. 4). When syn-tectonic minerals were absent, sense of movement was established by RM



and P-only criteria (Petit, 1987; Fig. 4) and by offset markers. Additionally, the orientation of 50 dikes and 109 veins and hydrothermal breccias were obtained.

Preferred orientations of faults, dikes and veins were analyzed using the software Stereonet (Allmendinger et al., 2012). Kinematic and dynamic analyses of the fault plane database were also completed. The aim of the first one is to establish the orientation of the compression and tension axes for each individual fault plane and the average kinematic axes (shortening, stretching and intermediate axes) for different fault populations. This was achieved using the FaultKin software (Allmendinger et al., 2012). Regarding the dynamic analysis, the Multiple Inverse Method (Yamaji, 2000) was used to calculate the orientation of paleo-stress tensors from the inversion of fault-slip data. The advantage of this method is that it allows the identification of separate stress states from heterogeneous data sets. A stress state is defined by four parameters: the orientation of the three principal stresses and the stress ratio $\Phi = (\sigma_2 - \sigma_3)/(\sigma_1 - \sigma_3)$. The stress ratio varies from 0 to 1, and describes the shape of the stress ellipsoid.

Two U-Pb LA-ICP-MS zircon ages were obtained at the Geochronology Laboratory of SERNAGEOMIN, the Chilean geological survey. Analytical procedures are detailed in Appendix 1.

4 Results

The structural database obtained from the 82 structural stations was used to establish the preferred orientations of fault planes, veins and dikes, and also to complete kinematic and dynamic analyses with the aim of establishing the prevailing strain axes and stress tensors in different segments of the PFS and conjugate faults and during successive reactivation events.

To achieve this aim, the study area was subdivided into five sectors (Fig. 5), each of them characterized by specific lithologies and structural patterns.

The Clarillo-La Obra sector (Fig. 5) includes structural stations located along one of the main WNW-striking branches of the PFS; the affected lithologies correspond to the early Miocene La Obra batholith and the Abanico Formation volcanic rocks.

Two new U-Pb zircon ages were obtained for this study (Table 1, analytical data in Appendix 2), from samples collected from different facies of the La Obra batholith, a major intrusive complex which is bounded to the south by the PFS but it is also affected by younger reactivations of it, and from which no previous U-Pb crystallization ages have been documented.

Tera-Wasserburg plots for the dated samples are shown in Fig. 6. The two samples are representative of the two main facies of the La Obra batholith. Sample FP01 correspond to an equigranular, medium- to coarse-grained, biotite-rich granodiorite, which is the most typical lithofacies of the intrusive complex. This sample yielded an age of 20.79 ± 0.13 Ma. Sample FP03 correspond to a hornblende-rich monzogranite, which is finer grained than the granodiorite, and it is exposed at the westernmost outcrops of the batholith. The calculated age of 20.69 ± 0.07 Ma from this sample is almost identical to the main granodioritic body.

These ages confirm that La Obra is the southernmost early Miocene intrusive complex of central Chile; to the south of the PFS, all the outcropping plutonic complexes in the Main Cordillera are middle Miocene or younger (Piquer et al., 2017, and references there in).



The Piuquencillo alto and Piuquencillo-Claro sectors (Fig. 5) are located in the Piuquencillo river valley, where the PFS was defined (Rivera and Falcon, 2000). In the Piuquencillo alto sector, the main lithological units are different intrusive facies of
130 Miocene plutons, which are emplaced in volcanic rocks of the middle Miocene Teniente Volcanic Complex. The Piuquencillo-Claro sector, in turn, is dominated by volcanic and volcanoclastic rocks of the Abanico and Coya-Machalí Formations, intruded by small-scale andesitic and dacitic-andesitic stocks and dikes. According to regional-scale stratigraphic interpretations (Piquer et al., 2017) the PFS correspond to the transition zone between these two units, with the Coya-Machalí Formation present only towards the south of this structure.

135 The San Pedro de Nolasco and Maipo sectors are located along a less notorious, WNW-striking branch of the PFS, and also contain traces of major NE-striking faults (Fig. 5). The San Pedro de Nolasco sector in particular includes the Ag-Pb-Zn-Cu vein system of the same name. The strike of individual veins varies from ENE to WNW, but the whole vein system defines a WNW-trending belt, 1.5 km long and 200 m wide. The veins are composed of quartz, calcite and barite with a sulphide ore of galena, sphalerite, tennantite/tetrahedrite, chalcopyrite and bornite (Leal, 2018). The polymetallic veins of San Pedro de
140 Nolasco are emplaced in volcanic rocks of the Teniente Volcanic Complex, which in the area overlay volcanic rocks of the Farellones Formation (Fig. 7). The Maipo sector contains mostly Abanico Formation volcanic rocks, intruded by small-scale stocks and dikes, some of them probably related to the middle Miocene San Gabriel pluton, located towards the north.

4.1 Preferred orientations

Figure 8 illustrates the preferred orientations of dikes/main intrusive contacts, veins/main hydrothermal breccia contacts, and
145 faults.

Dikes and intrusive contacts, and also veins and hydrothermal breccias show trends varying from ENE to NNW, with a remarkable absence of strikes approaching a N-S orientation. Regarding orientation of fault planes, the strong influence of the PFS is clearly visible, with a remarkable WNW preferred orientation, parallel to the general tendency of the PFS. Also visible is a secondary trend of ENE-striking fault planes, and a minor group of NNW-striking faults. Similar to the case of the veins
150 and hydrothermal breccias, there is a remarkable scarcity of N-S striking fault planes.

Figure 9 shows the preferred orientations of fault planes for the five different sectors into which the study area was subdivided for statistical analyses. Although the presence of large populations of WNW-striking fault planes related to the PFS is evidenced in all the five sectors, some remarkable differences are visible between them. The Piuquencillo-Claro sector, where the PFS was defined, shows the strongest dominance of WNW-striking fault planes. The Piuquencillo Alto and San Pedro de
155 Nolasco sectors clearly show the influence of an ENE-striking fault system, apart from the PFS. The Clarillo-La Obra sector marks the presence of a NNE-striking set of fault planes, while in the Maipo area, the influence of a NE-striking fault system is evident, which probably correspond to the Yeso Valley fault system (Fig. 2).

In 54 fault planes it was possible to obtain reliable kinematic information. A variety of syn-tectonic hydrothermal minerals were observed, including tourmaline, calcite, hematite, epidote and actinolite (Fig. 4). They are particularly common within
160 and in the vicinity of plutonic complexes. The orientation of all the 54 fault planes, their slickenlines and sense of movement



are shown in Fig. 10, while Fig. 11 shows the same information for each individual sector. Clarillo-La Obra sector is not shown, as no reliable kinematic data was obtained in this area. Preferred orientations of fault planes with kinematic information (Figs. 10, 11) are similar to the ones obtained from the total fault plane database (Figs. 8, 9), with a strong WNW preferred orientation, a secondary group striking ENE, and a minor population of fault planes striking NNW. Slickenlines most commonly show low pitch angles, indicating predominantly strike-slip movements.

5 Discussion

5.1 Kinematic and dynamic analysis

When considering all the 54 fault planes for which there is kinematic information available, it is evident that the sense of movement of most of the faults is consistent with fault activity under a strike-slip regime, with ENE-directed, sub-horizontal shortening and N-S to NNW-directing, sub-horizontal stretching. This is shown by the orientation of the average pressure and tension axis in the kinematic analysis and by the main clusters of σ_1 and σ_3 in the dynamic analysis (Fig. 10). However, the kinematic analysis (Fig. 10) shows an important dispersion of individual pressure and tension axes, suggesting a relatively heterogeneous deformation, in which the movement of several fault planes is not compatible with the average shortening (pressure) and stretching (tension) axes. The dynamic analysis, using the Multiple Inverse Method (Fig. 10), allows the distinction of secondary clusters of σ_1 and σ_3 , both of them vertical, showing that some groups of fault planes were active under extensional and compressional conditions respectively.

As discussed before, and shown by Figure 8, most of the measured fault planes have a WNW orientation, while the veins are more evenly distributed between WNW and ENE orientations. This could be related to the predominant ENE trend of σ_1 : as the ENE faults are more parallel to σ_1 , they are more efficient as fluid pathways, in contrast to WNW to NNW-striking faults, which are at higher angles relative to σ_1 and require higher fluid pressure or transient stress reversals to open and allow the circulation of fluids.

Similar kinematic and dynamic analyses were completed for the five sectors shown in Figure 5, and also for different lithological units. The latter was done to explore temporal variations in the stress state and strain axis, by looking at the variability in the results of the analysis for faults cross-cutting rocks of different ages. The lithological units considered were the Abanico and Coya-Machalí Formations; The Farellones Formation and the Teniente Volcanic Complex; subvolcanic intrusions; and the Miocene plutons. The results of this analyses are presented in Figures 12 to 15.

The kinematic and dynamic analysis of fault plane data by sector shows some remarkable differences between the upper and lower part of the Piuquencillo river valley. In the upper part of the valley (Piuquencillo alto), faults were active under a pure strike-slip regime (Fig. 13), while in the lower part (Piuquencillo-Claro), a transpressive (transitional between strike-slip and compressive) tectonic regime was predominant, showing very low Φ values and a large variability in the orientation of σ_3 (Fig. 13). This could be reflecting a trend from purely strike-slip regime in the central part of the Abanico/Coya-Machalí basin, to a transpressive regime predominant closer to the basin margins, already observed in regional studies (Piquer et al., 2016).



When considering the kinematic and dynamic analysis by lithological units, it is observed that the largest variability in the orientation of the principal stresses is observed in the volcanic units (Fig. 15), probably reflecting local variations in the stress state. The tectonic (far-field) stress tensor is more clearly defined in the intrusive units. The differences in the Φ value (Fig. 15) directly reflect the geographic position of the intrusive units: the predominant stress tensor calculated for faults in the Miocene plutons is identical to the one calculated for the Piuquencillo alto sector (Fig. 13), while the stress tensor calculated for subvolcanic intrusions is very similar to the one calculated for the Piuquencillo-Claro sector, where most of those intrusions are located.

200 5.2 Fault orientations and the flow of magmas and hydrothermal fluids

As discussed before and shown by Figure 8, it is evident that both WNW-striking faults, belonging to the PFS, and conjugate ENE-striking faults were capable of channeling magmas and hydrothermal fluids, as reflected in the preferred orientations of dikes and, particularly, hydrothermal veins and breccias. Syn-mineral displacement of the faults was mainly dextral for ENE- to NE-striking faults, sinistral for WNW-striking faults, and sinistral-reverse for NNW-striking faults. As also noted before, ENE-striking faults were the most favorably oriented for opening under the calculated predominant stress regime (E-W to ENE-trending σ_1), which explains why ENE-striking veins are as common as those striking WNW, while ENE-striking fault planes are much less frequent (Fig. 8). NNW-striking fault segments of the PFS in particular are the least favorable for opening under the predominant stress regime. This could make them highly attractive for mineral exploration, as they will tend to remain sealed for large periods of time, accumulating volatiles and allowing magmas to differentiate at depth, until fault reactivation occurs (perhaps triggered by co-seismic stress reversals, Mpodozis and Cornejo, 2012) creating instant permeability along the fault and allowing the rapid (often catastrophic) ascent of differentiated magmas and hydrothermal fluids. This is very clearly observed in the Río Blanco-Los Bronces porphyry Cu-Mo cluster, in which hydrothermal breccias and dacitic porphyries are emplaced along a NNW-striking fault system, while most of the late quartz veins and andesitic dikes are emplaced along NE-striking faults, more favorable for opening (Mpodozis and Cornejo, 2012; Piquer et al., 2015).

215 5.3 Beyond the PFS: the Maipo Deformation Zone

Our new field data demonstrate that the PFS can be traced across the entire Western Main Cordillera (Fig. 16) of Central Chile. However, Yáñez et al. (2002) proposed that the PFS might be part of a larger, continental-scale discontinuity, the Maipo Deformation Zone (Fig. 16). Several recent works completed in the coastal ranges near Valparaíso (Fig. 16), after the work of Yáñez et al. (2002) was published, confirm that the PFS can be extended to the NW across the entire continental margin. Evidences for the existence of a deep, long-lived, NW-striking fault system in the coastal ranges are varied. Creixell et al. (2011) showed that different Jurassic intrusions were syn-tectonically emplaced along NW-striking faults, under both sinistral transtension and transpression. In the same area, the structural architecture of the Upper Jurassic Antena Au vein district (Townley et al., 2000), is also dominated by NW-striking faults, which control the location of the mineralized district together with a system of conjugate, NE-striking faults. More to the SE, a similar situation occurs at the Early Cretaceous Lo Aguirre



225 stratabound Cu deposit (Fig. 16): the orebody has a very strong NW elongation, while post-mineral faults strike NE (Saric et
al., 2003). The latter appear to be also part of a large-scale structure, as they are on strike of a set of major NE-striking faults
identified in the Western Main Cordillera (the Saladillo, Flores and El Salto fault systems, Piquer et al., 2015), in the vicinity
of the Río Blanco-Los Bronces porphyry Cu-Mo cluster (Fig. 16). Subsequently, Rivera (2017) showed that this NW-striking
230 fault system is associated with regional-scale geological discontinuities in the coastal ranges. To the north of it, there is a
continuous N-trending belt of Jurassic sedimentary and volcanic units (Ajial, Cerro Calera and Horqueta Formations), and
Paleozoic rocks are absent. To the south, outcrops of Jurassic stratigraphic units and plutons are highly discontinuous, and the
geology of the coastal ranges is dominated by late Paleozoic intrusions and isolated blocks of metamorphic rocks
(SERNAGEOMIN, 2002; Rivera, 2017; see Fig. 16). Yáñez and Rivera (2019) proposed the existence of a series of
continental-scale discontinuities in the Chilean continental margin, which they defined as TLFs (Trans-Lithospheric Faults).
235 The concept of a TLF is equivalent to the fundamental basement structures of McCuaig and Hronsky (2014). According to the
interpretation of Yáñez and Rivera (2019), Lo Aguirre was emplaced at the intersection of two TLFs: the Valparaíso-Volcán
Maipo TLF, which coincides with the Maipo Deformation Zone (including the PFS), and the Aconcagua-San Antonio TLF,
which includes the NE-striking fault systems identified in Lo Aguirre and at the Río Blanco-Los Bronces district. These areas
of intersection of major fundamental basement structures develop complex interference patterns dominated by abundant
240 secondary faults and fractures, and therefore are associated with high permeability, being favorable sites for the emplacement
of mineral deposits. Also, it is common that these intersecting, continental-scale faults define wedge-shaped blocks with
distinctive stratigraphy and internal deformation styles (Piquer et al., 2019).

Within the study area, at the Clarillo-La Obra and Piuquencillo/Piuquencillo-Claro sectors (Fig. 5), the PFS coincides with a
major change in the deformation style of the Cenozoic infill of the inverted Abanico Basin. Towards the south, the Miocene
245 Coya-Machalí Formation crop out, and this unit is strongly deformed by a series of tight folds and reverse faults, constituting
the Cordón Perales fold and thrust belt (Rivera, 2017). The fold axes of these folds are interrupted by the PFS, and to the north
of it, the Coya-Machalí Fm. is absent (Fig. 2) and the older, Eocene-Oligocene Abanico Formation is more gently folded.

Towards the SE of the study area, the PFS is associated with major changes in the orientation and vergence of the N- to NNE-
striking fault systems that define the boundary between the Western and Eastern Main Cordillera, at the inverted eastern margin
250 of the Paleogene Abanico Basin (Fig. 16; Rivera, 2017). Moreover, the seismic activity related to these arc-parallel faults is
much more intense to the south of their intersection with the PFS than to the north of it, and a very large cluster of seismic
activity appears at the intersection zone (see Fig. 3 of Piquer et al., 2019). Even though we cannot rule out other reasons to
explain the differences in seismic activity, among them differences in recording time window and/or differences in water
percolation between both sectors. Further SE, in the Eastern Main Cordillera, the prolongation of the PFS is at least spatially
255 related to the Escalones prospect (Fig. 16), a Cu skarn deposit emplaced in Lower Cretaceous marine sedimentary rocks, with
a well-developed skarn alteration mineralogy, and high hypogene Cu grades (Maksaev et al., 2007). There is no published
information about the local-scale structural controls on mineralization at Escalones, but the Lower Cretaceous calcareous beds
strike NW, parallel to the PFS (Maksaev et al., 2007). To the SE of Escalones, the PFS follows the northern margin of the



Diamante Caldera, a major Pleistocene collapse structure (Stern et al., 1984; Harrington, 1989) within which the Maipo
260 stratovolcano (Fig. 16) is located.

There is also evidence that some segments of the MDZ are tectonically active. Sabaj (2008) identified and characterized
potentially active faults in the Coastal ranges of central Chile. It was concluded that fault architecture in the area is dominated
by NW-striking faults, intersected by different sets of NE-striking faults. At least four of the individual NW-striking faults
recognized in the work of Sabaj (2008) are located within the Maipo Deformation Zone, on-strike of the PFS: the Marga-
265 Marga, Valparaíso, Laguna Verde and Valparaíso-Curacaví faults. They were later grouped in the Valparaíso Fault System
(VFS) by Del Valle (2018). Both the NW- and NE-striking faults were concluded to be potentially active by Sabaj (2008),
although the NW-striking faults were considered to pose the higher risk, as their traces are more continuous and longer. It was
estimated that the maximum possible magnitude (M_w) of seismic events generated by the NW-striking faults is between 5.8
and 7.1. The seismic hazard posed by these NW-striking faults in the Andean forearc was confirmed by the activation of the
270 Pichilemu fault, located ~140 km to the south of the MDZ, after the M_w 8.8 subduction earthquake of 27 February 2010 (Farías
et al., 2011; Aron et al., 2013). The Pichilemu fault was activated on 11 March, 12 days after the main interplate earthquake,
and produced two main shocks, M_w 6.9 and 7.0 (Farías et al., 2011; Aron et al., 2013). Focal mechanisms indicate normal
movement of the SW-dipping Pichilemu fault (Farías et al., 2011; Aron et al., 2013), consistent with the expected relaxation
of NW-striking crustal faults (normally under compression) during the co- and post-seismic periods. In the Main Cordillera,
275 there is no direct evidence of neotectonic activity of the PFS, but similar, WNW-striking faults have been shown to displace
Quaternary terraces of the Maipo river, ~25 km to the north of the PFS (Lavenu and Cembrano, 2008). One of the focal
mechanism solutions of the Las Melosas earthquake, a major (M_w 6.9) intraplate seismic event registered in 1958 in the Main
Cordillera, less than 10 km to the north of the PFS, is compatible with activity along a WNW-striking fault (Alvarado et al.,
2009). If this was the case, it is most likely that this earthquake was generated by one of the northernmost branches of the PFS.
280 However, the other possible solution, represented by a NNE-striking fault plane, is equally plausible, considering the presence
of several individual faults with NE- to NNE-strike near Las Melosas (Piquer et al., 2019).

Considering the fact that both the PFS in the Main Cordillera and the VFS in the fore-arc are potentially active, it is worth
noting that the southern part of the city of Santiago is built on top of the MDZ, between the PFS and the VFS. The Santiago
valley is covered by unconsolidated sedimentary and volcanic deposits (SERNAGEOMIN, 2002; Fig. 16). Yáñez et al. (2015),
285 based on detailed gravimetric modelling, showed that the topography of the basement of the Santiago valley presents large-
scale breaks and scarps which coincide with the expected position of major branches of the MDZ, and also with other, NE-
striking faults. The assessment of the neotectonic activity of the MDZ-related faults, their recurrence intervals and the risk
they pose to the Santiago and Valparaíso urban areas are highly relevant topics, which require further studies and evaluation.
As shown in Fig. 16, there is a second continental-scale structural system sub-parallel to the PFS and the Maipo Deformation
290 Zone, located immediately to the south of it. This second fault system, from east to west, defines the southern boundary of the
Diamante caldera, it has been well recognized at the El Teniente porphyry Cu-Mo district (Piquer et al., 2016; Fig. 16), and it
is also well defined at the Coastal ranges and plains of central Chile (SERNAGEOMIN, 2002; Fig. 16), passing through the



port city of San Antonio. Here we will refer to this structure as the Teniente-San Antonio fault system. This major fault system and the Maipo Deformation Zone might be the manifestations in the present-day surface of the same continental scale
295 discontinuity at depth; however, testing this possibility is beyond the scope of this work.

There are also geophysical evidences that highlights the relevance of the PFS, the broader Maipo Deformation Zone, and also the Teniente-San Antonio fault system. Yáñez et al. (1998) defined the Melipilla anomaly, a large-scale, WNW-striking negative magnetic anomaly located in the coastal area of central Chile (Fig. 17), which coincides with the western segment of the Teniente-San Antonio fault system. To the north of the Melipilla anomaly, a second, NW-striking negative magnetic
300 anomaly is also evident (Fig. 17), and coincides with the western segment of the Maipo Deformation Zone. These negative magnetic anomalies most likely correspond to felsic Paleozoic and Mesozoic intrusive bodies, emplaced along these long-lived fault systems.

Finally, a different type of manifestation of these continental-scale structures might have been observed during the Valparaíso seismic sequence of 2017 (Nealy et al., 2017). The distribution of the hypocenters of the multiple earthquakes registered during
305 this event (Fig. 17) shows a clear NW alignment, and is neatly bounded by the submarine prolongation of the Maipo Deformation Zone and the Teniente-San Antonio fault system. The earthquakes are strongly concentrated at the plate boundary mega-thrust (Nealy et al., 2017), so they were not generated by the activation of crustal faults. However, the remarkable spatial relationship between earthquake distribution and large-scale faults in the continental lithosphere shown in Fig. 17, might indicate the existence of a still poorly understood feedback mechanism between large-scale, trans-lithospheric discontinuities
310 in the upper plate and the distribution of subduction-related earthquake sequences at the plate boundary.

6 Conclusion

- The continuity and surface expression of the PFS across all the Western Main Cordillera is confirmed
- During the middle to late Miocene, the PFS was active with sinistral to sinistral-reverse kinematics, under a strike-slip to transpressive tectonic regime with sub-horizontal, E-W to ENE-trending σ_1
- 315 - Both the PFS and conjugate, ENE-striking faults, channelled the flow of magmas and syn-tectonic hydrothermal fluids. The ENE-striking faults were more efficient pathways for hydrothermal fluids than the PFS
- A lower Miocene crystallization age (20.9-20.6 Ma, U-Pb in zircons) is confirmed for the La Obra pluton, which is bounded to the south by the PFS
- The PFS corresponds to the expression in the Western Main Cordillera of a continental-scale fundamental basement
320 structure (Fig. 16), which has been called the Maipo Deformation Zone or the Valparaíso-Volcán Maipo trans-lithospheric fault. This structure has been active at least since the Jurassic, controlling the flow of magmas and hydrothermal fluids, and at least some of its segments are still tectonically active today
- The surface expression of pre-Andean, lithospheric-scale fault systems is often very subtle, but they can be characterized through multidisciplinary studies involving, among others, detailed structural field work and geophysical
325 interpretations. The study of this type of long-lived fault systems is a relevant task, as they strongly control the distribution



and geometry of both fossil and active magmatic-hydrothermal systems, and they can be reactivated with different kinematics during the seismic cycle; the seismic hazard associated with this structures requires more detailed evaluations

Author contribution

330 José Piquer and Nicolás Oyarzún completed the field work and the analysis of fault plane data. Orlando Rivera participated actively in the interpretation of structural and stratigraphic data, providing inputs based in his earlier works at the Piuquencillo Fault System. Gonzalo Yáñez completed the geophysical interpretations. José Piquer prepared the manuscript with important contributions from the co-authors, mainly Orlando Rivera and Gonzalo Yáñez.

Acknowledgments

335 Founding for the first two field campaigns completed as part of this work came from the DID project S-2016-32, an internal research project from Universidad Austral de Chile titled “El Sistema de Falla Piuquencillo: evolución y control sobre el emplazamiento de sistemas hidrotermales”. The logistics and costs involved on the third field campaign were covered by the Rio Tinto mining company. All the analytical costs were covered by DID project S-2016-32.

References

- 340 Aguirre, L.: Geología de los Andes de Chile Central, Provincia de Aconcagua, Instituto de Investigaciones Geológicas, Santiago, Chile, 70 pp., 1960.
- Allmendinger, R.W., Cardozo, N., and Fisher, D.M.: Structural Geology Algorithms: Vectors and Tensors, Cambridge University Press, New York, United States of America, 2012.
- Alvarado, P., Barrientos, S., Sáez, M., Astroza, M., and Beck, S.: Source study and tectonic implications of the historic 1958 Las Melosas crustal earthquake, Chile, compared to earthquake damage, *Physics of the Earth and Planetary Interiors*, 175 (1-2), 26-36, 2019.
- 345 Aron, F., Allmendinger, R.W., Cembrano, J., González, G., and Yáñez, G.: Permanent fore-arc extension and seismic segmentation: Insights from the 2010 Maule earthquake, Chile, *Journal of Geophysical Research: Solid Earth*, 118, 1-16, doi: 10.1029/2012JB009339, 2013.
- Cembrano, J. and Lara, L.: The link between volcanism and tectonics in the southern volcanic zone of the Chilean Andes: A review, *Tectonophysics*, 471, 96-113, doi: 10.1016/j.tecto.2009.02.038, 2009.
- 350 Charrier, R., Baeza, O., Elgueta, S., Flynn, J. J., Gans, P., Kay, S. M., Munoz, N., Wyss, A. R., and Zurita, E.: Evidence for Cenozoic extensional basin development and tectonic inversion south of the flat-slab segment, southern Central Andes, Chile (33° -36° SL), *Journal of South American Earth Sciences*, 15 (1), 117-139, 2002.
- Chernicoff, C.J., Richards, J.P., Zappettini, E.O.: Crustal lineament control on magmatism and mineralization in northwestern Argentina: geological, geophysical, and remote sensing evidence, *Ore Geology Reviews*, 21, 127-155, 2002.



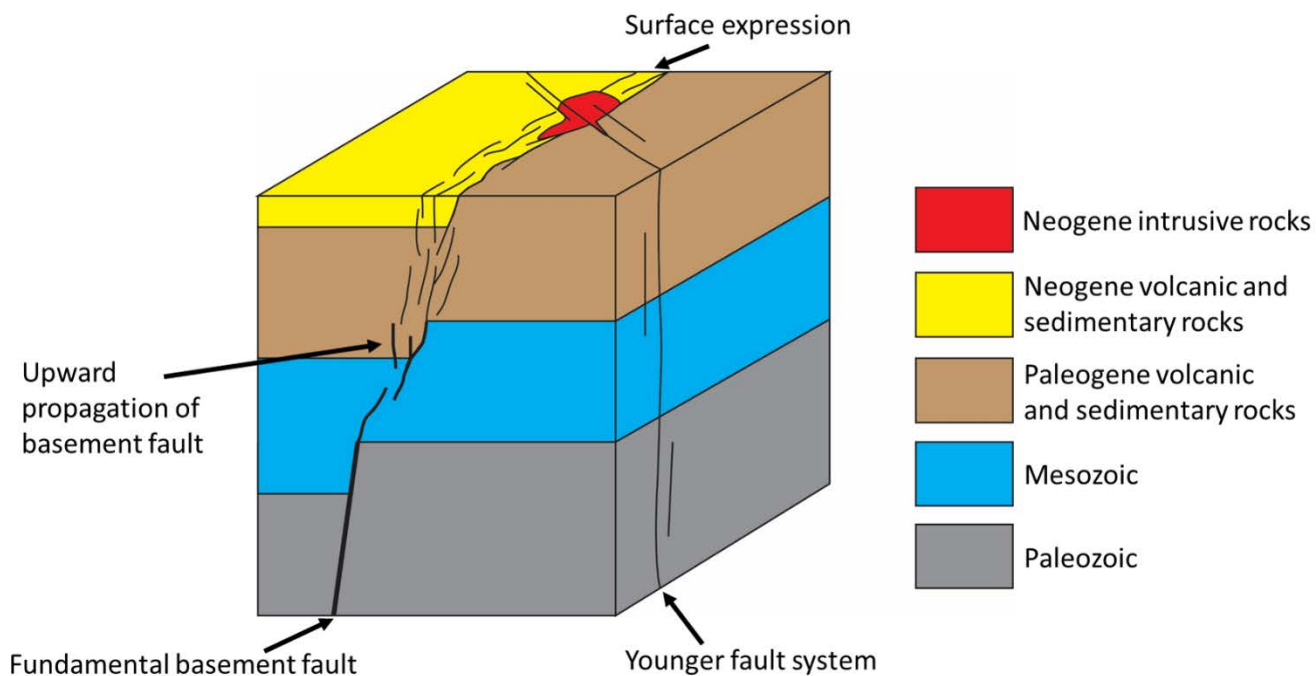
- Creixell, C., Parada, M.A., Morata, D., Vásquez, P., Pérez de Arce, C., and Arriagada, C.: Middle-Late Jurassic to Early Cretaceous transtension and transpression during arc building in Central Chile: evidence from mafic dike swarms, *Andean Geology*, 38, 37-63, 2011.
- Del Valle, F., Marquardt, C., Valdivia, D., Elgueta, S., and Yáñez, G.: Tasa de alzamiento neotectónico del margen costero entre Los Vilos y Santo Domingo, in: *Proceedings of the 15th Chilean Geological Congress*, Concepción, Chile, 18-23 November 2018, 1305-1307, 2018.
- 360 Farías, M., Comte, D., Roecker, S., Carrizo, D., and Pardo, M.: Crustal extensional faulting triggered by the 2010 Chilean earthquake: The Pichilemu Seismic Sequence, *Tectonics*, 30, doi:10.1029/2011TC002888, 2011.
- Fock, A.: Cronología y tectónica de la exhumación en el Neógeno de los Andes de Chile Central entre los 33° y los 34°, undergraduate thesis, Departamento de Geología, Universidad de Chile, Chile, 179 pp., 2005.
- 365 Fuentes, F., Aguirre, L., Vergara, M., Valdebenito, L., and Fonseca, E.: Miocene fossil hydrothermal system associated with a volcanic complex in the Andes of central Chile, *Journal of Volcanology and Geothermal Research*, 138, 139-161, 2004.
- Godoy, E.: Geología del área entre los ríos Claro del Maipo y Cachapoal, CODELCO Chile-SERNAGEOMIN, Santiago, Chile, 68 pp., 1993.
- 370 Harrington, R.: The Diamante Caldera and Maipo Caldera Complex in the southern Andes of Argentina and Chile (34°10' South), *Revista de la Asociación Geológica Argentina*, 44 (1-4), 186-193, 1989.
- Jackson, S.E., Pearson, N.J., Griffin, W.L., and Belousova, E.A.: The application of laser ablation-inductively coupled plasma-mass spectrometry to in situ U-Pb zircon geochronology, *Chemical Geology*, 211, 47-69, 2004.
- Kay, S.M., Godoy, E., and Kurtz, A.: Episodic arc migration, crustal thickening, subduction erosion, and magmatism in the south-central Andes, *Geological Society of America Bulletin*, 117, 67-88, doi: 10.1130/B25431.1, 2005.
- 375 Klohn, C.: Geología de la Cordillera de los Andes de Chile Central, Instituto de Investigaciones Geológicas, Santiago, Chile, 95 pp., 1960.
- Lavenu, A. and Cembrano, J.: Quaternary compressional deformation in the Main Cordillera of Central Chile (Cajón del Maipo, east of Santiago), *Revista Geológica de Chile*, 35, 233-252, doi: 10.5027/andgeoV35n2-a03, 2008.
- 380 Leal, D.: Caracterización y origen del Sistema de vetas de San Pedro de Nolasco, Cordillera Principal de la Región Metropolitana, Chile central, undergraduate thesis, Instituto de Ciencias de la Tierra, Universidad Austral de Chile, Chile, 124 pp., 2019.
- Maksaev, V., Townley, B., Palacios, C., and Camus, F.: Metallic ore deposits, in: *Geology of Chile*, edited by: Moreno, T. and Gibbons, W., The Geological Society, London, United Kingdom, 179-199, 2007.
- 385 McCuaig, T.C. and Hronsky, J.M.A.: The mineral system concept: the key to exploration targeting, *Society of Economic Geologists Special Publication*, 18, 153-176, 2014.
- Mpodozis, C. and Cornejo, P.: Cenozoic tectonics and porphyry copper systems of the Chilean Andes, *Society of Economic Geologists Special Publication*, 16, 329-360, 2012.



- Nealy, J.L., Herman, M.W., Moore, G.L., Hayes, G.P., Benz, H.M., Bergman, E.A., and Barrientos, S.E.: 2017 Valparaíso
390 earthquake sequence and the megathrust patchwork of central Chile, *Geophysical Research Letters*, 44, 8865–8872, doi:
10.1002/2017GL074767, 2017.
- Petit, J.P.: Criteria for the sense of movement on fault surfaces in brittle rocks, *Journal of Structural Geology*, 9 (5/6), 597-
608, 1987.
- Piquer, J., Skarmeta, J., and Cooke, D.R.: Structural evolution of the Rio Blanco-Los Bronces district, Andes of central Chile:
395 controls on stratigraphy, magmatism and mineralization, *Economic Geology*, 110, 1995–2023, doi:
10.2113/econgeo.110.8.1995, 2015.
- Piquer, J., Berry, R.F., Scott, R.J., and Cooke, D.R.: Arc-oblique fault systems: their role in the Cenozoic structural evolution
and metallogenesis of the Andes of central Chile, *Journal of Structural Geology*, 89, 101–117, doi: 10.1016/j.jsg.2016.05.008,
2016.
- 400 Piquer, J., Hollings, P., Rivera, O., Cooke, D.R., Baker, M., and Testa, F.: Along-strike segmentation of the Abanico Basin,
central Chile: new chronological, geochemical and structural constraints, *Lithos*, 268, 174–197, doi:
10.1016/j.lithos.2016.10.025, 2017.
- Piquer, J., Yáñez, G., Rivera, O., and Cooke, D.R.: Long-lived crustal damage zones associated with fault intersections in the
high Andes of Central Chile, *Andean Geology*, 46 (2), 223–239, doi: 10.5027/andgeoV46n2-3106, 2019.
- 405 Richards, J.P., Boyce, A.J., and Pringle, M.S.: Geologic evolution of the Escondida area, northern Chile: a model for spatial
and temporal localization of porphyry Cu mineralization, *Economic Geology*, 96, 271–305, 2001.
- Rivera, O.: Marco geodinámico para los pórfidos cupríferos Mio-Pliocenos de Chile central: rol de estructuras translitosféricas
y anomalías gravimétricas en la metalogénesis Andina, M. Sc. thesis, Departamento de Ciencias Geológicas, Universidad
Católica del Norte, Chile, 214 pp., 2017.
- 410 Rivera, O. and Falcón, M. F.: Secuencias de relleno de cuencas volcano-tectónicas transversales Oligo-Miocenas en los
alrededores del yacimiento El Teniente (33°45' - 34°30' LS), in: *Proceedings of the 9th Chilean Geological Congress*, Puerto
Varas, Chile, 31 July–04 August 2000, 819–823, 2000.
- Sabaj, R.: Identificación y caracterización de estructuras potencialmente activas en la cordillera de la costa entre los 33° y
33°45' S, undergraduate thesis, Departamento de Geología, Universidad de Chile, Chile, 92 pp., 2008.
- 415 Salfity, J.A.: Lineamientos transversales al rumbo andino en el noroeste argentino, in: *Proceedings of the 4th Chilean
Geological Congress*, Antofagasta, Chile, 19–24 August 1985, 119–137, 1985.
- Saric, N., Kreft, C., and Huete, C.: Geología del yacimiento Lo Aguirre, Chile, *Revista Geológica de Chile*, 30 (2), 317–331,
2003.
- SERNAGEOMIN: Carta Magnética de Chile 1:250.000, Santiago sheet, Servicio Nacional de Geología y Minería, Santiago,
420 1 map, 1980.
- SERNAGEOMIN: Mapa Geológico de Chile 1:1.000.000, Servicio Nacional de Geología y Minería, Santiago, Carta
Geológica de Chile, Serie Geología Básica 75, 1 map in 3 sheets, 2002.



- Stern, C.R., Amini, H., Charrier, R., Godoy, E., Hervé, F., and Varela, J.: Petrochemistry and age of rhyolitic pyroclastic flows which occur along the drainage valleys of the río Maipo and río Cachapoal (Chile) and the río Yaucha and río Papagayos (Argentina), *Revista Geológica de Chile*, 23, 39-52, 1984.
- 425 Thomas, H.: Informe de la comisión geológica Thomas-Junge sobre la alta cordillera entre el río Aconcagua y el río Colorado, CORFO, Santiago, Chile, 76 pp., 1953.
- Townley, B., Makshev, V., Palacios, C., Hernández, T., Hurtado, R., Jorquera, R., and Gonzalez, E.: Mineralización aurífera en la Cordillera de la Costa en Chile central: distritos Antena (V Región) y Colliguay (Región Metropolitana), in Proceedings of the 9th Chilean Geological Congress, Puerto Varas, Chile, 31 July-04 August 2000, 171-175, 2000.
- 430 Weinreb, R.W. and Hasert, M.: Bathymetric Charts of the South East Pacific with links to gridded datasets, PANGAEA, <https://doi.org/10.1594/PANGAEA.785515>, 2012.
- Yamaji, A.: The multiple inverse method: a new technique to separate stresses from heterogeneous fault-slip data, *Journal of Structural Geology*, 22, 441-452, 2000.
- 435 Yáñez, G. and Rivera, O.: Crustal dense blocks in the fore-arc and arc region of Chilean ranges and their role in the magma ascent and composition: Breaking paradigms in the Andean metallogeny, *Journal of South American Earth Sciences*, 93, 51-66, doi: 10.1016/j.jsames.2019.04.006, 2019.
- Yáñez, G., Gana, P., and Fernández, R.: Origen y significado geológico de la Anomalía Melipilla, Chile central, *Revista Geológica de Chile*, 25 (2), 175-198, 1998.
- 440 Yáñez, G., Cembrano, J., Pardo, M., Ranero, C., and Sellés, D.: The Challenger-Juan Fernández-Maipo major tectonic transition of the Nazca-Andean subduction system at 33-34°S: geodynamic evidence and implications, *Journal of South American Earth Sciences*, 15, 23-38, 2002.
- Yáñez, G., Muñoz, M., Flores-Aqueveque, V., and Bosh, A.: Gravity derived depth to basement in Santiago Basin, Chile: implications for its geological evolution, hydrogeology, low enthalpy geothermal, soil characterization and geo-hazards, *Andean Geology*, 42, 147-172, doi: 10.5027/andgeoV42n2-a01, 2015.
- 445

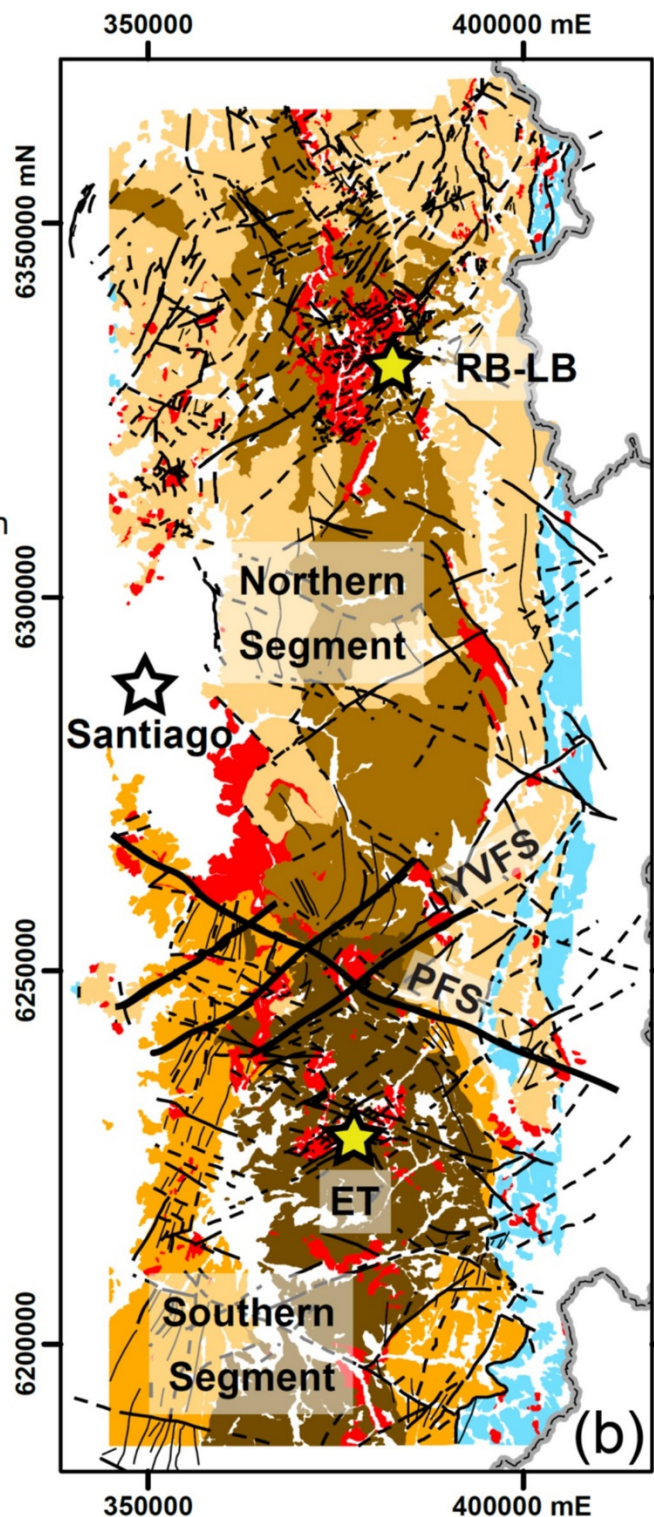
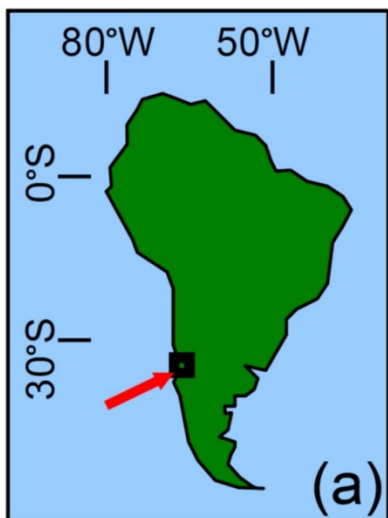


450 **Figure 1: Schematic diagram showing how Fundamental Basement Structures (FBSs) propagate upwards through younger rocks, being represented at the current surface by a network of minor faults, often difficult to recognize in the field. The diagram also illustrates the common re-activation of this type of faults as basin-bounding faults under extensional conditions, and the relationship between fundamental basement faults and the emplacement of intrusive complexes. A younger, cross-cutting fault system is also illustrated. Adapted from Figure 7 of McCuaig and Hronsky (2014) and Figure 9 of Piquer et al. (2019).**



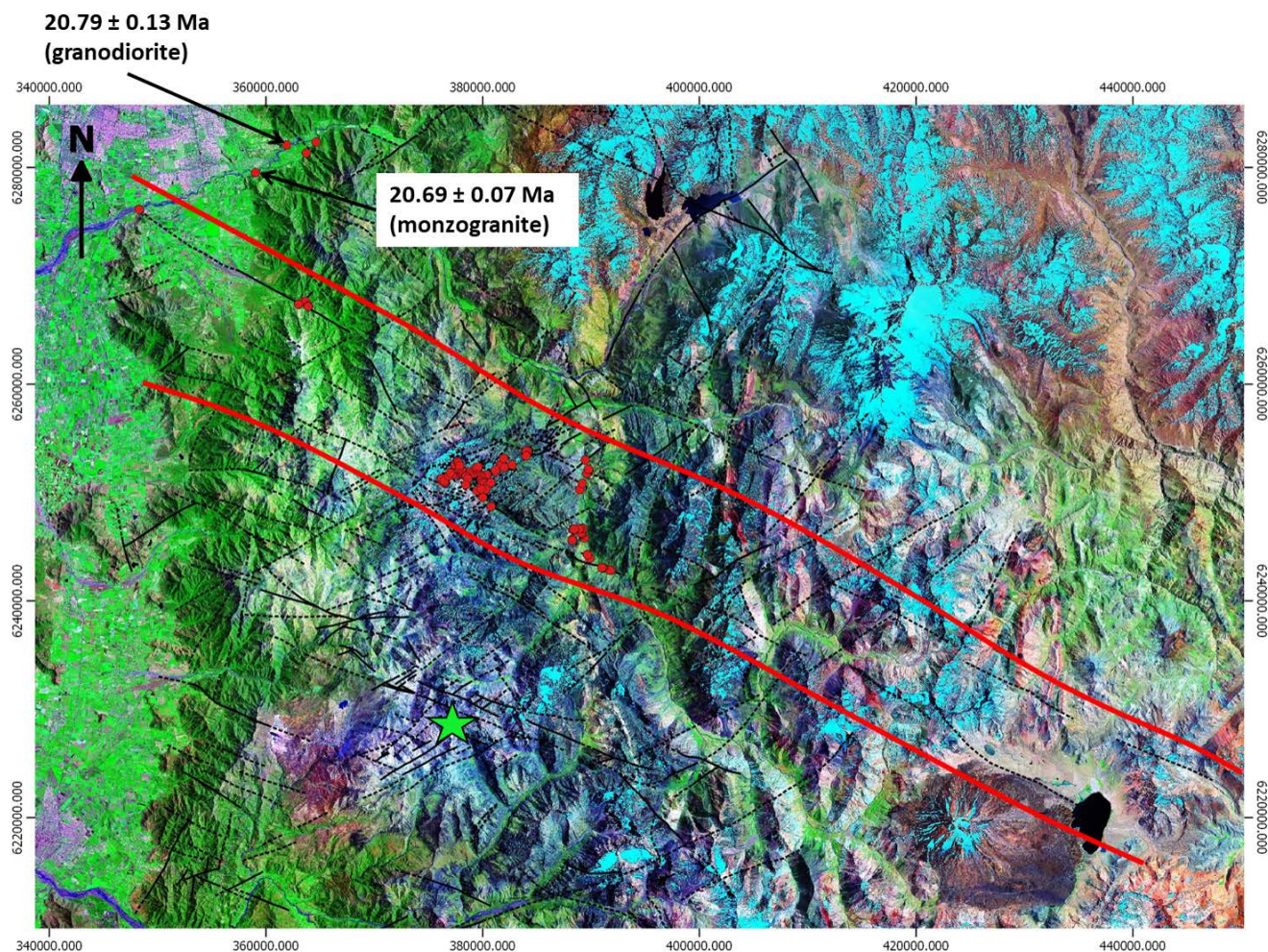
Legend (map b)

- Chile-Argentina border
- Quaternary sediments and volcanic deposits
- Tertiary intrusive rocks
- Teniente Volcanic Complex
- Farellones Formation
- Coya-Machali Formation
- Abanico Formation
- Mesozoic sedimentary rocks
- Inferred fault
- Fault
- Fold

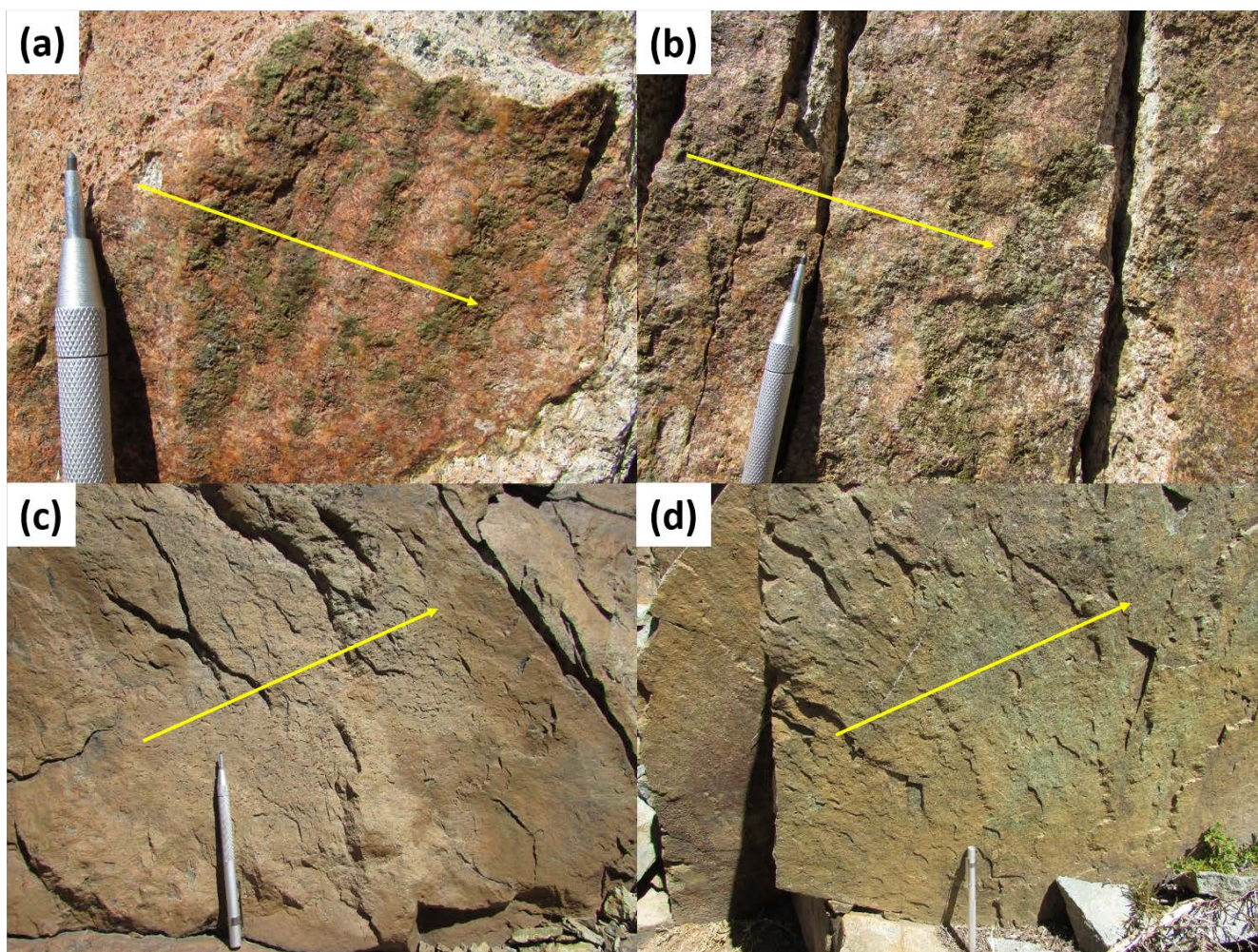




455 **Figure 2: A. Location of the study area in South America. B. Geology of the Andes of central Chile, based on Rivera and Falcón (2000), SERNAGEOMIN (2002), Fuentes et al. (2004), Fock (2005) and this work. Quaternary sediments and volcanic deposits not shown. PFS = Piuquencillo Fault System, YVFS = Yeso Valley Fault System, RB-LB = Río Blanco – Los Bronces, ET = El Teniente.**



460 **Figure 3: Distribution of structural stations (red dots) and sample location for U-Pb zircon ages. Red lines show the approximate boundary of the PFS; green star shows the location of the El Teniente porphyry Cu-Mo deposit. The background correspond to a Landsat image, courtesy of the U.S. Geological Survey.**



465 **Figure 4:** Fault planes in different branches of the PFS. All of them show evidences of sinistral strike-slip movements. (a) and (b) correspond to fault planes affecting Miocene plutons, with syn-tectonic epidote (a) and actinolite (b). (c) and (d) correspond to fault planes affecting volcanic rocks of the Teniente Volcanic Complex, with sense of movement indicated by RM criteria (Petit, 1987).

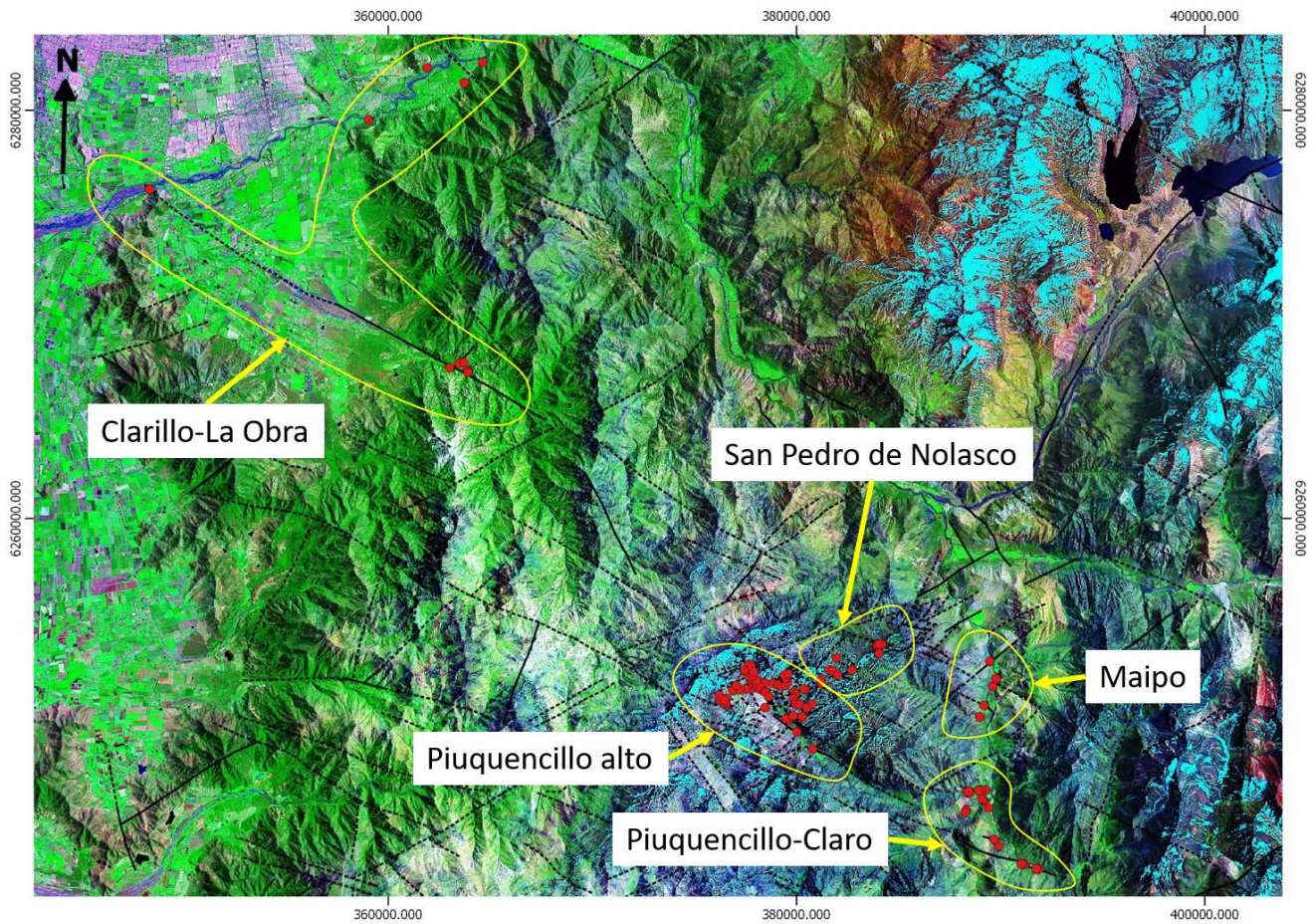
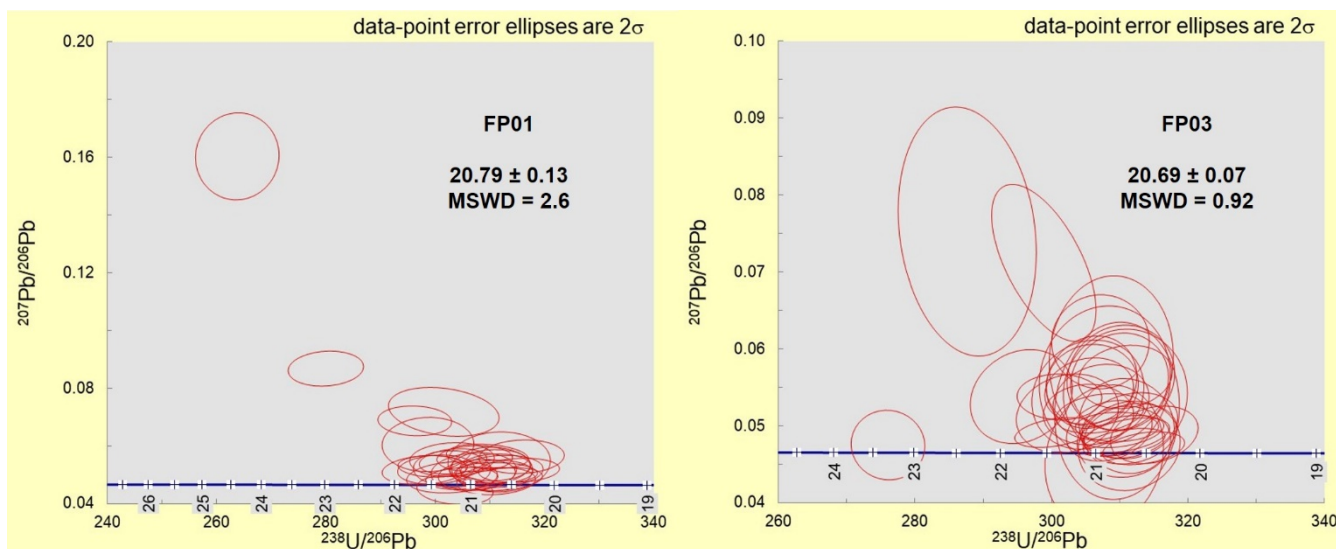


Figure 5: Subdivision of the study area into five sectors for the analysis of preferred orientations and the calculation of strain axes and stress tensors. The background correspond to a Landsat image, courtesy of the U.S. Geological Survey.



470 **Figure 6:** Tera-Wasserburg plots for the two U-Pb analyses completed for this study. Numbers on the reference concordia traces
are millions of years.



475 **Figure 7:** Unconformity separating the flat-lying Teniente Volcanic Complex (TVC) and the gently-folded Farellones Formation.
View west from the San Pedro de Nolasco vein area.

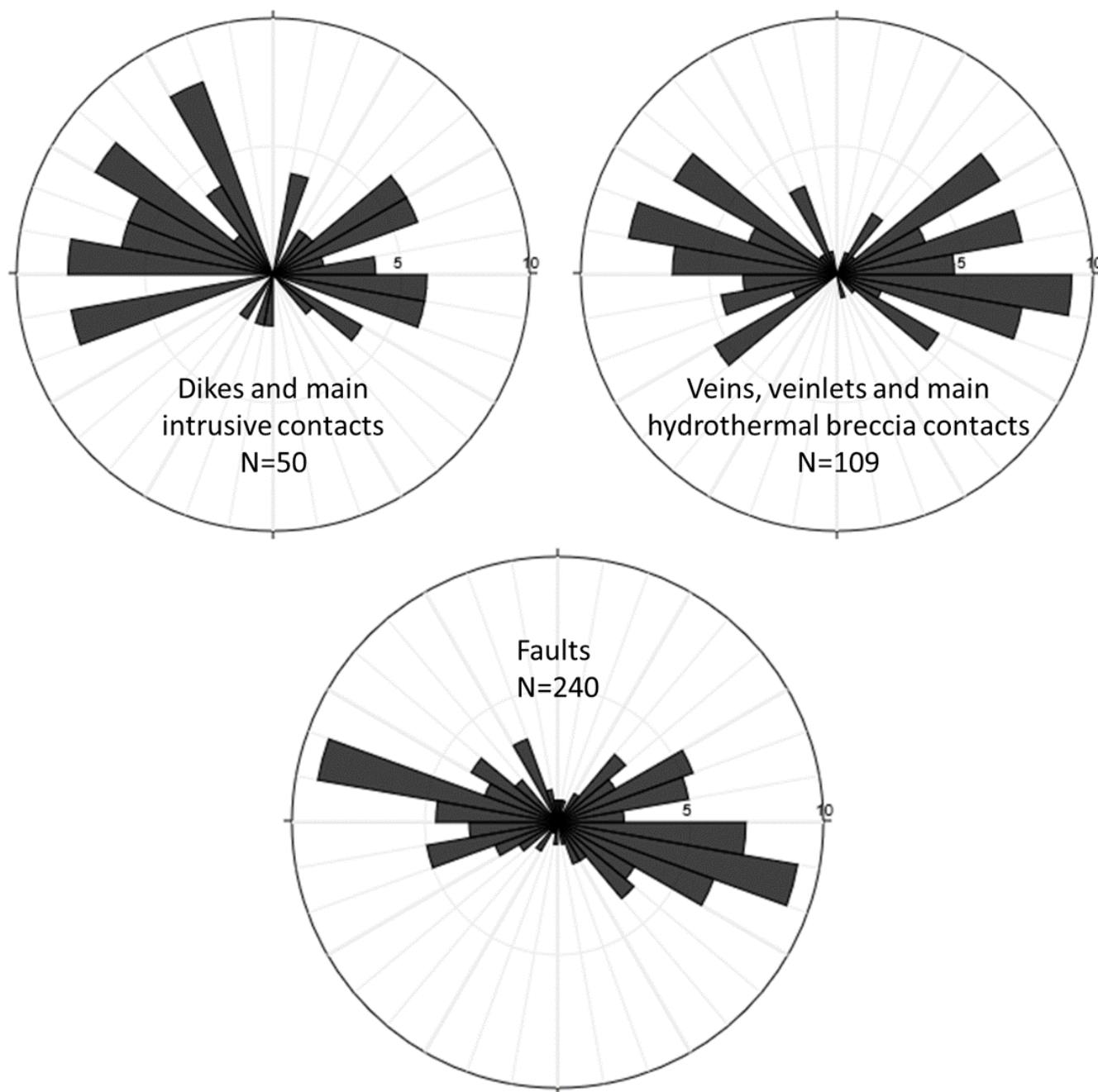
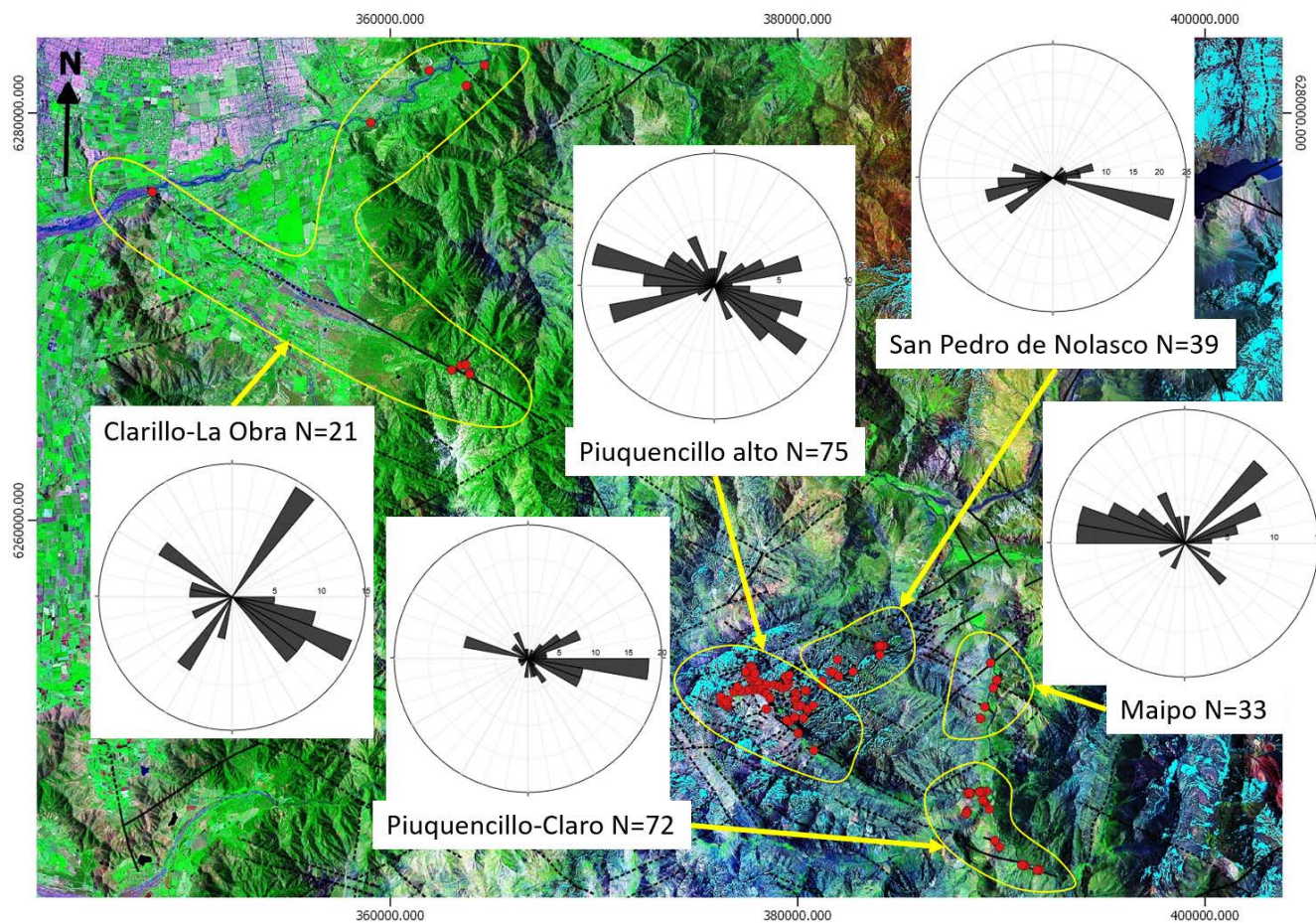
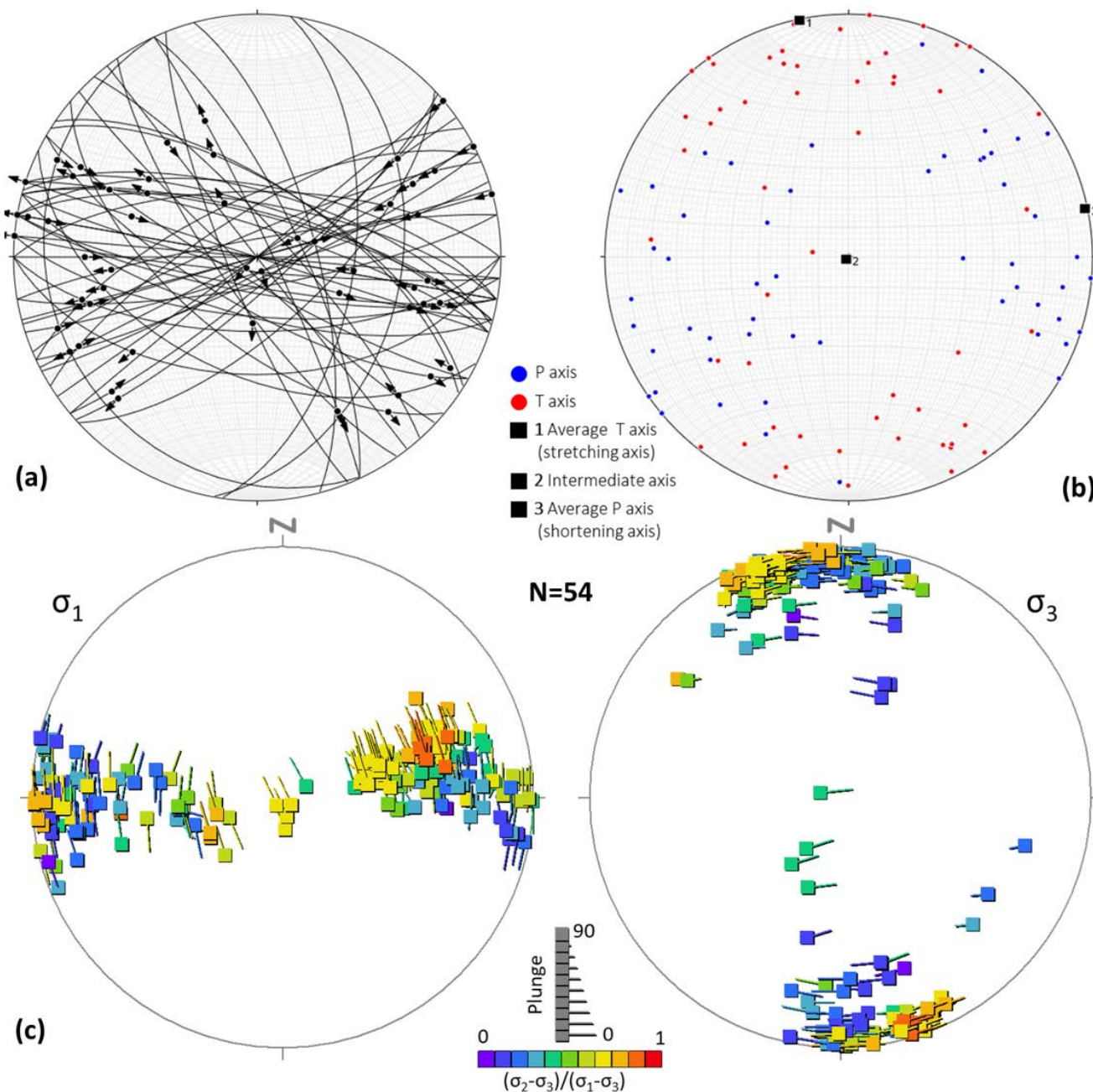


Figure 8: Preferred orientations of dikes/main intrusive contacts, veins/main hydrothermal breccia contacts and faults, for all the study area (82 structural stations).



480 **Figure 9:** Preferred orientations of fault planes in the five sectors into which the study area was subdivided. The background correspond to a Landsat image, courtesy of the U.S. Geological Survey.



485 **Figure 10:** (a) Lower-hemisphere, equal-area projection of the 54 fault planes with kinematic information, showing also the slickenline attitudes and the sense of movement. (b) Results of the kinematic analysis for the fault planes shown in (a). P = pressure, T = tension. (c) Results of the dynamic analysis for the fault planes shown in (a). Colors represent the Φ value calculated for each stress tensor.

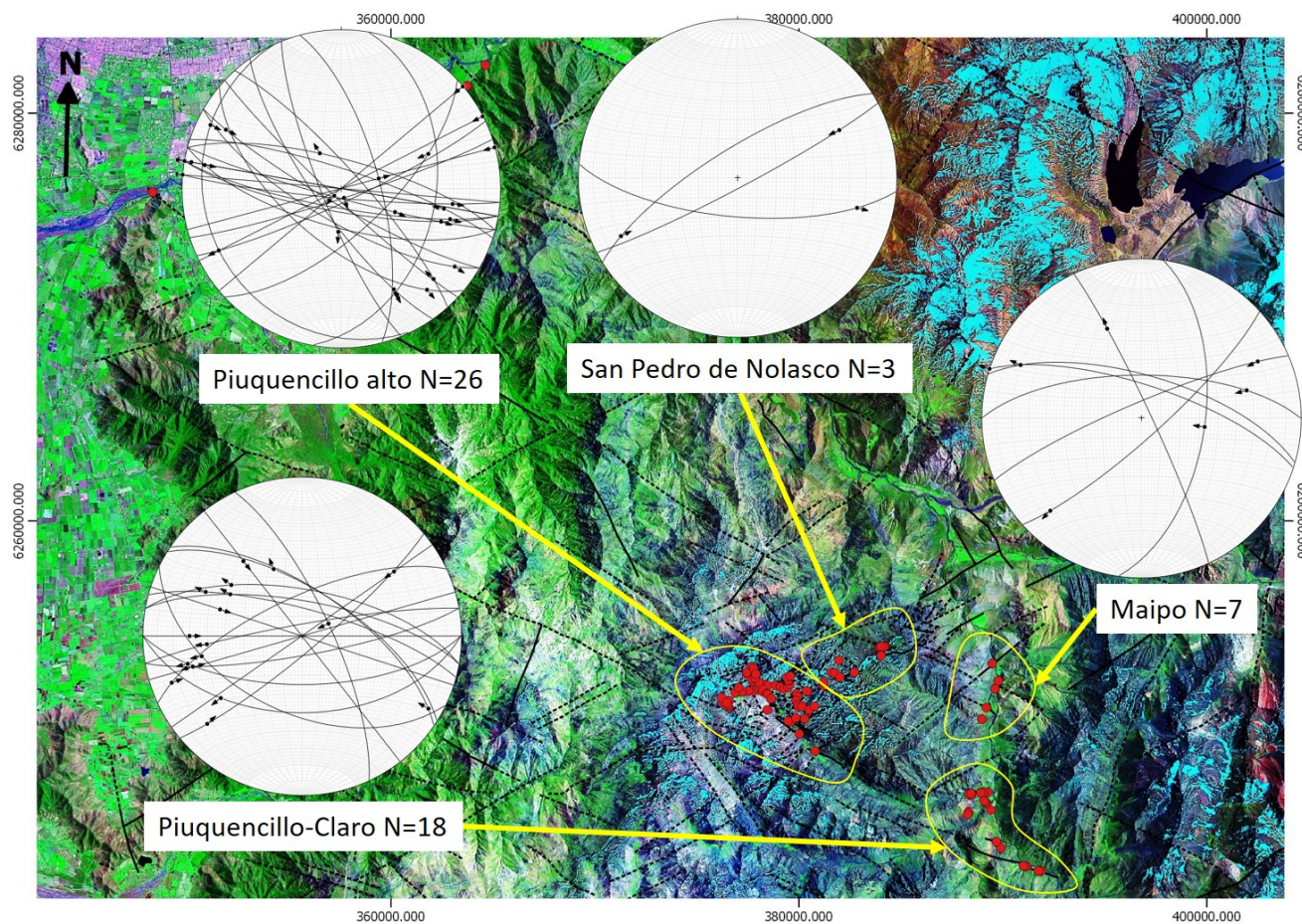


Figure 11: Lower-hemisphere, equal-area projection of the fault planes with kinematic information by sector, showing also the slickenline attitudes and the sense of movement. The background correspond to a Landsat image, courtesy of the U.S. Geological Survey.

490

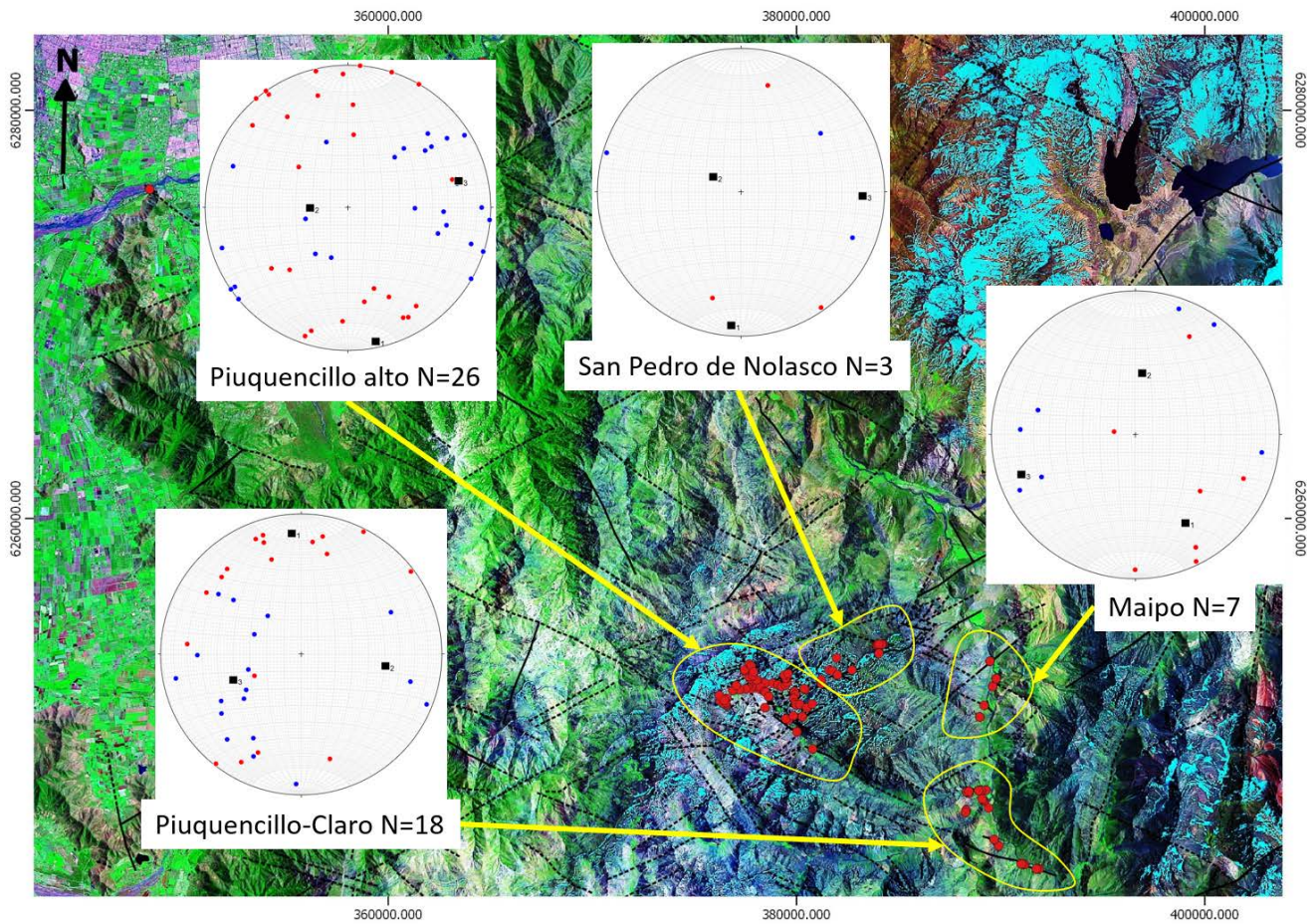
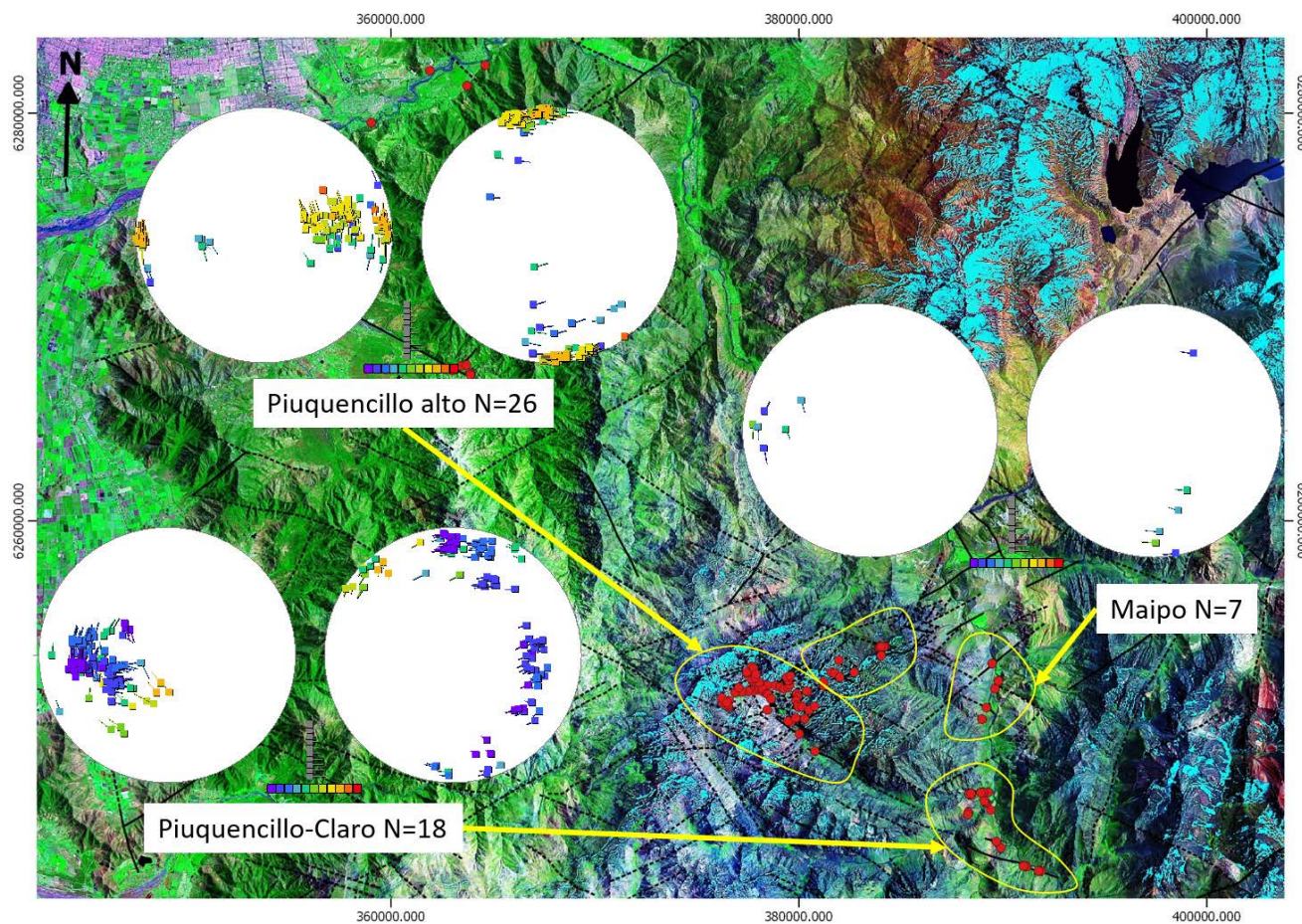
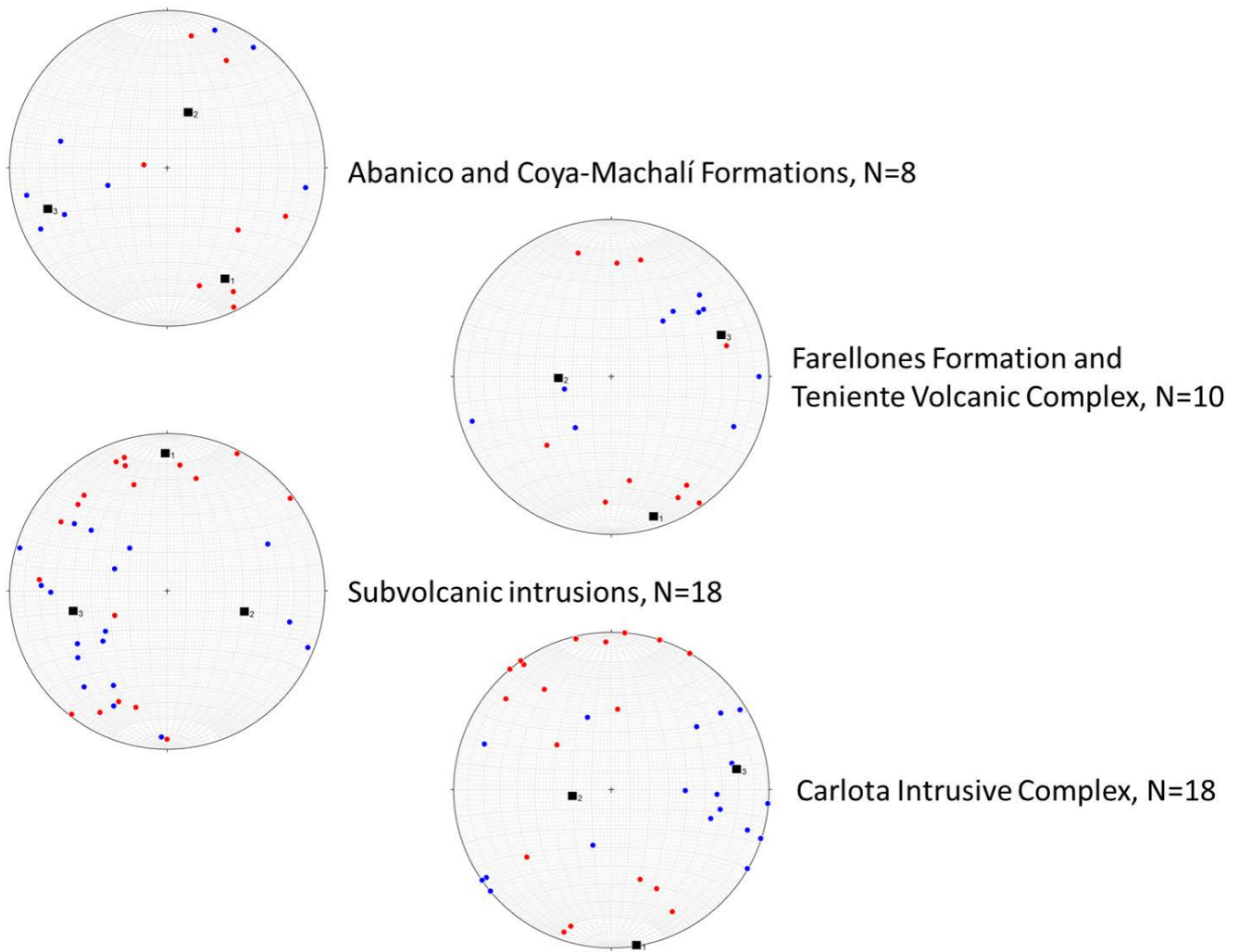


Figure 12: Kinematic analysis of fault plane data by sector. Clarillo-La Obra sector is not considered, as no reliable kinematic indicators were found. The background correspond to a Landsat image, courtesy of the U.S. Geological Survey.



495

Figure 13: Dynamic analysis of fault plane data by sector. Clarillo-La Obra and San Pedro de Nolasco sectors are not considered, as the minimum of four fault planes with reliable kinematic indicators, necessary for stress state calculations, was not achieved in these areas. The background correspond to a Landsat image, courtesy of the U.S. Geological Survey.



500 **Figure 14: Kinematic analysis of fault plane data by lithological unit.**

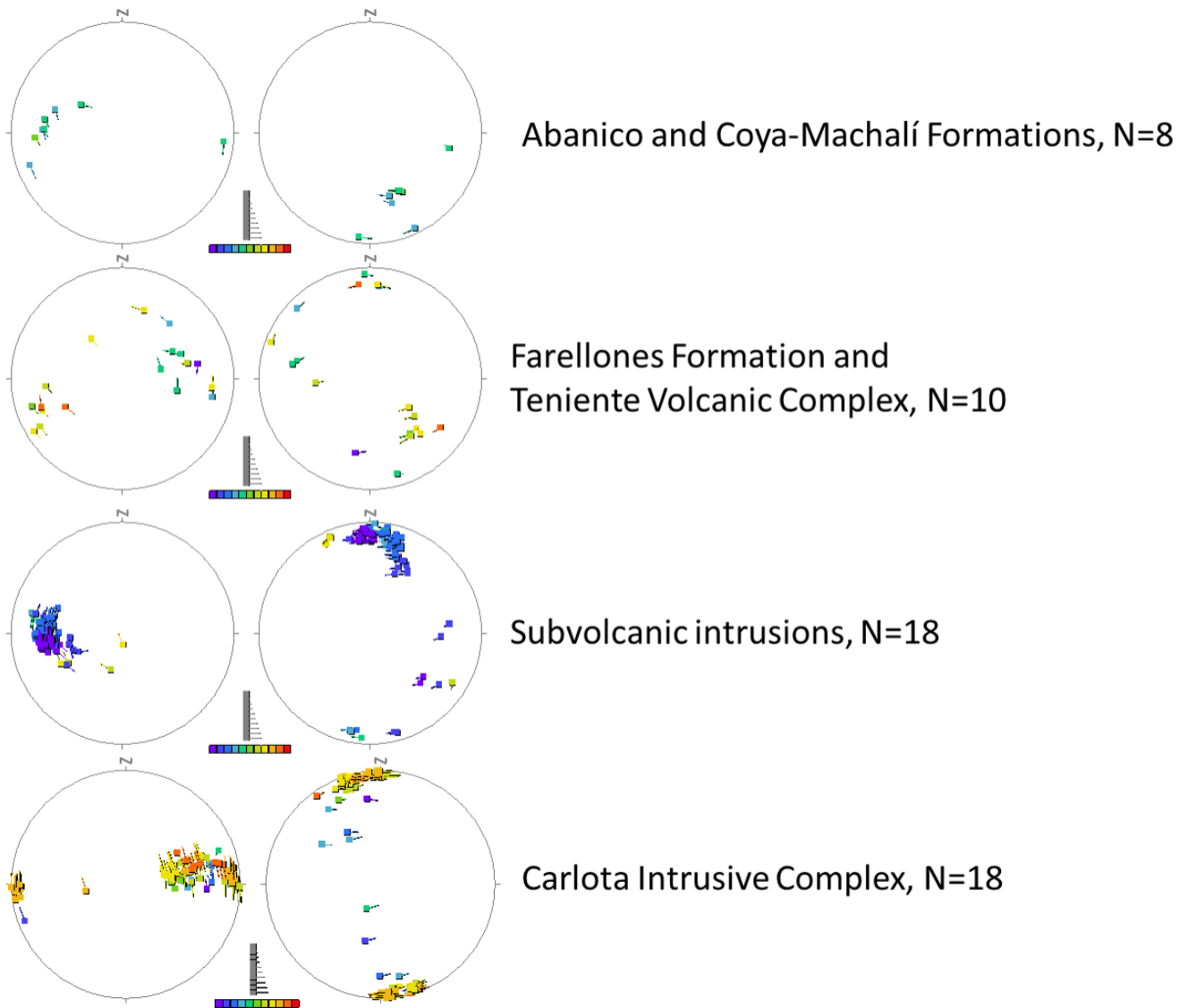
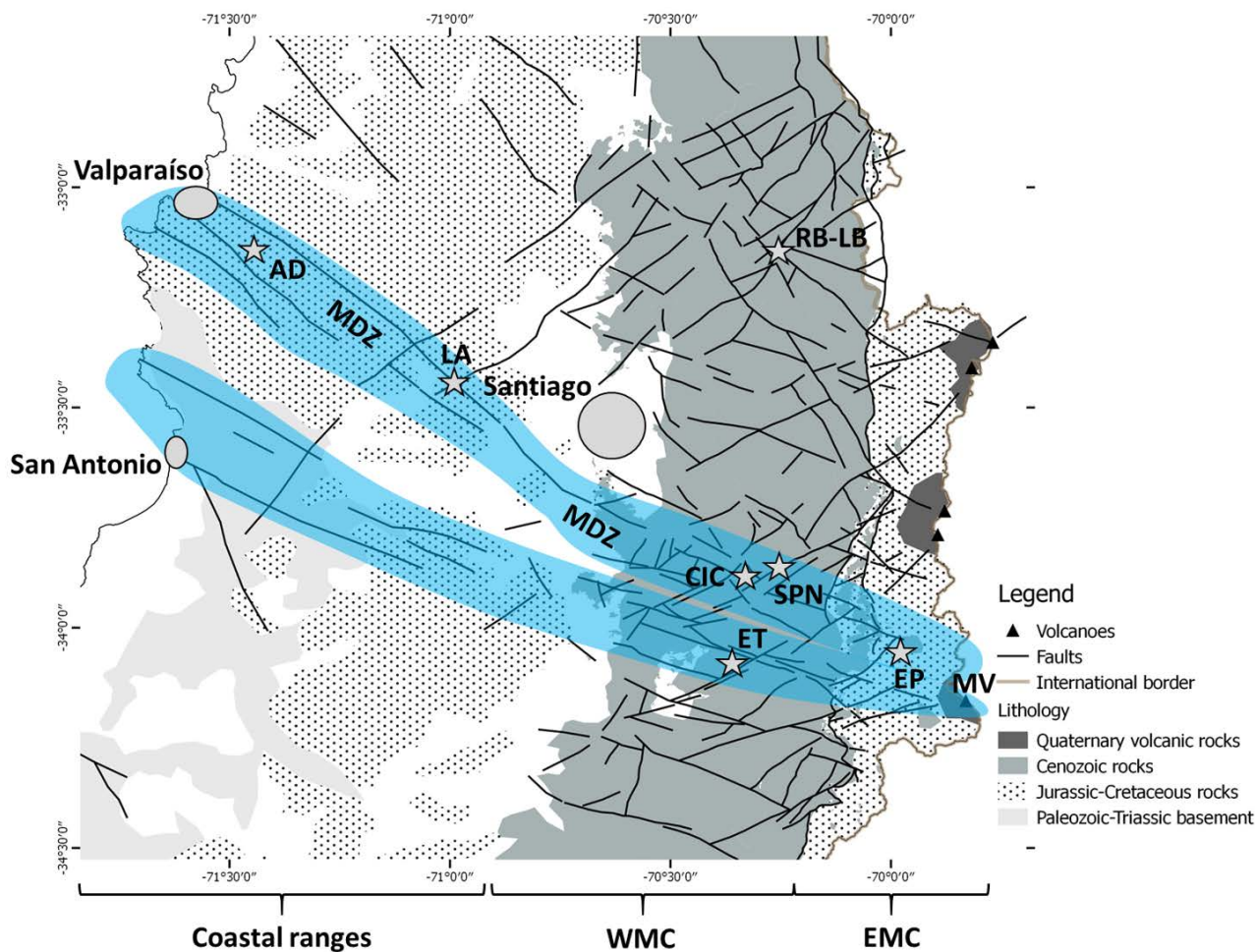
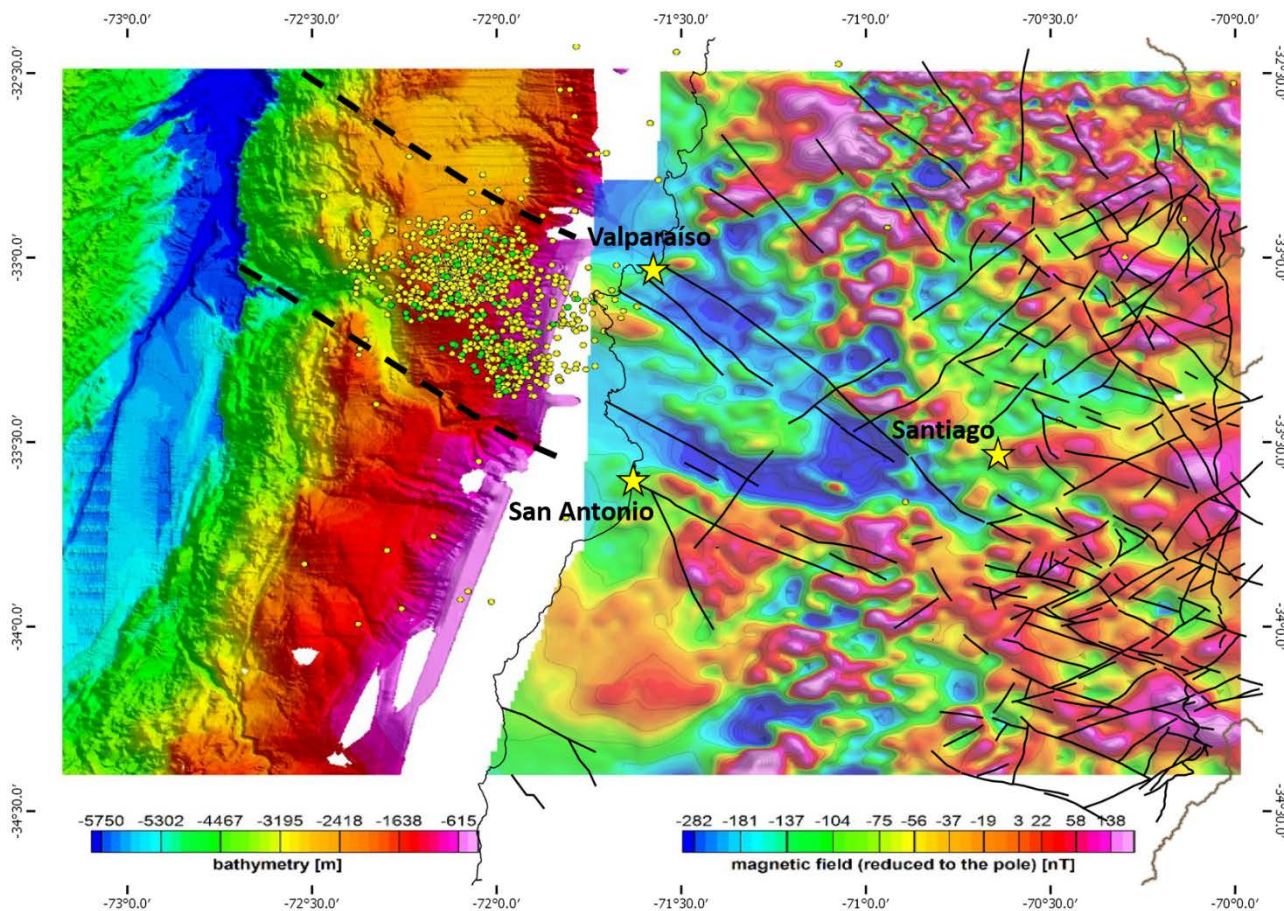


Figure 15: Dynamic analysis of fault plane data by lithological unit.



505 **Figure 16: Continental-scale expression of the Maipo deformation zone (MDZ), highlighted in light blue; the PFS correspond to its manifestation in the Cenozoic rocks of the Western Main Cordillera. Background geology from SERNAGEOMIN (2002); faults in the Western Main Cordillera from Piquer et al. (2016). RB-LB = Río Blanco-Los Bronces; ET = El Teniente; EP = Escalones prospect; SPN = San Pedro de Nolasco veins; CIC = Carlota Intrusive Complex; LA = Lo Aguirre stratabound deposit; AD = Antena District of orogenic Au veins; MV = Maipo Volcano; WMC = Western Main Cordillera; EMC = Eastern Main Cordillera. The main cities of Santiago and Valparaíso are also shown.**



510

515

Figure 17: Geophysical expressions of the PFS, the Maipo Deformation Zone and the Teniente-San Antonio fault system. The submarine continental shelf is colored according to its bathymetry (Weinrebe and Hasert, 2012); thick dashed lines represent the possible submarine prolongation of the two main branches of the MDZ. Colors in the continent correspond to RTP aeromagnetic map (SERNAGEOMIN, 1980). Yellow and green small circles show the location of earthquake hypocenters related to the 2017 Valparaíso sequence (yellow data set extracted from CSN data repository, green data set, relocated events from Nealy et al 2017, data repository). The Chile-Argentina international boundary, the coastline and fault architecture from Fig. 16 are also shown.

520



Sample	N (UTM)	E (UTM)	Lithology	Age (Ma) ($\pm 2\sigma$)	MSWD	Number of grains
			Biotite-rich			
FP01	6281776	361704	granodiorite	20.79 ± 0.13	2.6	29
			Hornblende-rich			
FP03	6279214	358835	monzogranite	20.69 ± 0.07	0.92	34

525 **Table 1: Summary of U-Pb zircon geochronology of the La Obra batholith.**

Appendix A: U-Pb geochronology analytical procedures

All the procedures described here were completed at the Geochronology Laboratory of SERNAGEOMIN (National Survey of Geology and Mining, Chile) at Santiago, Chile. First the samples were sieved and crushed using standard procedures to obtain a non-magnetic heavy mineral concentrate, from which zircon crystals were separated. The selected crystals were mounted in epoxy glue briquettes, and then studied at a Scanning Electron Microscope, with which back-scattered electron (BSE) and cathodoluminescence (CL) images were obtained.

At sample FP01, the selected zircon crystals vary in size between 100 and 300 μm approximately. They correspond to igneous zircons with oscillatory zoning, some of them showing evidences of inherited cores. No overgrowth was observed at crystal rims. The grains contain abundant inclusions and fractures, which required a careful selection of the lase ablation spots.

At sample FP03, the selected zircon crystals vary in size between 100 and 500 μm approximately. They correspond to igneous zircons with oscillatory zoning, without observed evidences of inherited cores. Overgrowth was observed at the rims of some crystals, and some of them display irregular borders, maybe as a result of hydrothermal processes. The grains contain very few inclusions and fractures.

After spot selection based on CL and BSE images, the analyses were completed using a Thermo Fischer ElementXR ICP-MS, coupled with a Photon-Machines Analyte G2 193 nm excimer laser, with a wavelength of 193 nm. U, Th and Pb concentrations were calculated in relation to the reference zircon GJ-1 (Jackson et al., 2004). Isotope ratios were normalized to the same reference zircon.

545



Appendix B: U-Pb geochronology analytical data

550 Values in bold correspond to those used for age calculations.

(1) Values not considered in the calculations due to an incorrect pattern in isotopic ratio curves (isotopic content inhomogeneity)

$^{206}\text{Pb}/^{238}\text{U}$ (corr by common Pb)		$^{206}\text{Pb}/^{238}\text{U}$		$^{207}\text{Pb}/^{235}\text{U}$		$^{207}\text{Pb}/^{206}\text{Pb}$			$^{207}\text{Pb}/^{206}\text{Pb}$
age	2 σ	ratio	2 σ	ratio	2 σ	Rho	ratio	2 σ	Common
FP01									
21.2	0.5	0.00330	0.00007	0.02233	0.00200	0.07485	0.04940	0.00450	0.83698
20.8	0.5	0.00326	0.00007	0.02291	0.00240	0.07219	0.05170	0.00520	0.83696
21.1	0.5	0.00335	0.00008	0.02791	0.00360	0.15235	0.06120	0.00730	0.83700
21.0	0.4	0.00330	0.00006	0.02483	0.00160	0.02329	0.05440	0.00340	0.83698
21.0	0.4	0.00328	0.00006	0.02204	0.00140	0.11814	0.04890	0.00300	0.83697
20.6	0.4	0.00322	0.00006	0.02310	0.00280	0.18976	0.05240	0.00600	0.83695
20.6	0.4	0.00323	0.00006	0.02339	0.00220	0.05477	0.05340	0.00490	0.83695
20.4	0.5	0.00321	0.00008	0.02406	0.00380	0.11754	0.05690	0.00820	0.83694
21.1	0.4	0.00338	0.00006	0.03196	0.00210	0.35555	0.06820	0.00410	0.83701
21.2	0.4	0.00329	0.00006	0.02031	0.00200	0.36009	0.04520	0.00410	0.83698
21.3	0.4	0.00334	0.00006	0.02435	0.00150	0.35256	0.05280	0.00270	0.83699
20.6	0.4	0.00321	0.00006	0.02243	0.00140	0.34455	0.05060	0.00280	0.83694
20.9	0.6	0.00379	0.00009	0.08384	0.00670	0.27281	0.16000	0.01100	0.83718
20.5	0.4	0.00321	0.00007	0.02262	0.00200	0.08329	0.05180	0.00450	0.83694
21.3	0.4	0.00333	0.00006	0.02377	0.00190	0.10277	0.05170	0.00400	0.83699
20.5	0.4	0.00321	0.00006	0.02262	0.00150	0.25837	0.05160	0.00310	0.83694
20.5	0.4	0.00320	0.00006	0.02137	0.00140	0.00231	0.04900	0.00310	0.83694
21.4	0.5	0.00336	0.00007	0.02387	0.00190	0.08780	0.05300	0.00410	0.83700
20.7	0.4	0.00325	0.00006	0.02493	0.00170	0.20271	0.05640	0.00360	0.83696
20.5	0.4	0.00322	0.00006	0.02329	0.00170	0.13290	0.05320	0.00340	0.83694
20.6	0.6	0.00332	0.00009	0.03282	0.00350	0.48085	0.07440	0.00730	0.83698
20.5	0.4	0.00323	0.00006	0.02512	0.00170	0.47512	0.05790	0.00340	0.83695



21.8	0.5	0.00357	0.00007	0.04274	0.00250	0.23171	0.08650	0.00450	0.83709
21.0	0.5	0.00330	0.00007	0.02512	0.00220	0.14942	0.05600	0.00450	0.83698
20.8	0.4	0.00325	0.00006	0.02243	0.00190	0.04361	0.05160	0.00440	0.83696
20.6	0.4	0.00321	0.00006	0.02118	0.00170	0.07506	0.04910	0.00380	0.83694
21.1	0.4	0.00330	0.00006	0.02368	0.00240	0.21186	0.05320	0.00550	0.83698
20.3	0.4	0.00317	0.00006	0.02252	0.00150	0.14284	0.05220	0.00330	0.83692
20.1	0.4	0.00317	0.00006	0.02454	0.00210	0.14760	0.05650	0.00470	0.83692
(1)		0.00387	0.00019	0.07508	0.02200	0.99260	0.11100	0.01800	
(1)		0.00434	0.00011	0.15304	0.01700	0.11226	0.25300	0.02700	
(1)		0.00378	0.00011	0.07912	0.00560	0.13594	0.15460	0.00980	
(1)		0.00437	0.00031	0.15016	0.03100	0.99093	0.21300	0.03000	
(1)		0.11283	0.02400	12.51304	2.80000	0.99880	0.78600	0.01100	

²⁰⁶Pb/²³⁸U (corr
 by common Pb)

²⁰⁶Pb/²³⁸U

²⁰⁷Pb/²³⁵U

²⁰⁷Pb/²⁰⁶Pb

²⁰⁷Pb/²⁰⁶Pb

age	2σ	ratio	2σ	ratio	2σ	Rho	ratio	2σ	Common
FP03									
21.2	0.4	0.00332	0.00006	0.02461	0.00120	0.37242	0.05350	0.00240	0.83699
20.8	0.4	0.00327	0.00006	0.02461	0.00160	0.14300	0.05490	0.00330	0.83697
20.8	0.4	0.00324	0.00005	0.02206	0.00140	0.01562	0.04990	0.00310	0.83695
20.5	0.5	0.00324	0.00008	0.02617	0.00400	0.11329	0.05880	0.00860	0.83695
20.7	0.4	0.00325	0.00006	0.02382	0.00180	0.11766	0.05460	0.00400	0.83696
20.5	0.4	0.00326	0.00006	0.02735	0.00230	0.21824	0.06300	0.00500	0.83696
20.6	0.4	0.00321	0.00006	0.02098	0.00210	0.09036	0.04790	0.00480	0.83694
21.6	0.5	0.00338	0.00007	0.02510	0.00230	0.05167	0.05220	0.00450	0.83701
21.6	0.7	0.00348	0.00010	0.03608	0.00660	0.31855	0.07500	0.01300	0.83705
20.5	0.5	0.00322	0.00007	0.02500	0.00250	0.12196	0.05680	0.00570	0.83695
21.1	0.4	0.00331	0.00007	0.02353	0.00190	0.08736	0.05190	0.00420	0.83698
20.6	0.4	0.00322	0.00006	0.02216	0.00230	0.23467	0.04990	0.00520	0.83694
20.5	0.5	0.00322	0.00008	0.02402	0.00310	0.16945	0.05490	0.00710	0.83694



20.9	0.5	0.00325	0.00008	0.02059	0.00340	0.00612	0.04550	0.00740	0.83696
20.7	0.3	0.00322	0.00005	0.02124	0.00058	0.06152	0.04790	0.00120	0.83694
20.5	0.4	0.00323	0.00006	0.02480	0.00230	0.11619	0.05540	0.00520	0.83695
20.5	0.4	0.00322	0.00006	0.02500	0.00150	0.16404	0.05520	0.00340	0.83694
20.8	0.4	0.00327	0.00006	0.02510	0.00220	0.07492	0.05570	0.00460	0.83697
20.5	0.3	0.00319	0.00005	0.02070	0.00073	0.09545	0.04770	0.00170	0.83693
20.4	0.3	0.00317	0.00005	0.02137	0.00130	0.03120	0.04900	0.00290	0.83693
20.7	0.3	0.00322	0.00005	0.02188	0.00071	0.09875	0.04910	0.00160	0.83695
20.6	0.6	0.00325	0.00008	0.02500	0.00360	0.11666	0.05670	0.00780	0.83696
21.3	0.3	0.00333	0.00005	0.02255	0.00068	0.12092	0.04930	0.00140	0.83699
20.6	0.4	0.00321	0.00006	0.02216	0.00150	0.02902	0.04970	0.00320	0.83694
20.8	0.4	0.00326	0.00006	0.02317	0.00092	0.15464	0.05220	0.00210	0.83696
20.6	0.3	0.00322	0.00005	0.02163	0.00074	0.01478	0.04890	0.00160	0.83694
20.6	0.6	0.00323	0.00008	0.02314	0.00420	0.07568	0.05300	0.01000	0.83695
20.8	0.5	0.00328	0.00007	0.02441	0.00260	0.06892	0.05510	0.00590	0.83697
20.8	0.4	0.00327	0.00006	0.02490	0.00200	0.18788	0.05500	0.00440	0.83697
20.9	0.4	0.00327	0.00006	0.02323	0.00150	0.25362	0.05170	0.00320	0.83697
20.9	0.5	0.00335	0.00007	0.03284	0.00430	0.70012	0.07090	0.00800	0.83700
20.6	0.4	0.00321	0.00006	0.02167	0.00140	0.07098	0.04920	0.00320	0.83694
20.7	0.3	0.00323	0.00005	0.02220	0.00077	0.43799	0.05020	0.00150	0.83695
20.7	0.4	0.00322	0.00006	0.02127	0.00170	0.16802	0.04790	0.00360	0.83694
23.3	0.4	0.00362	0.00006	0.02372	0.00190	0.23066	0.04750	0.00360	0.83711
(1)		0.00352	0.00009	0.05049	0.00650	0.53069	0.10300	0.01200	
(1)		0.00343	0.00010	0.05000	0.01000	0.91903	0.09400	0.01400	
(1)		0.00262	0.00006	0.01760	0.00093	0.06173	0.04910	0.00270	
(1)		0.00373	0.00007	0.03157	0.00200	0.07834	0.06150	0.00390	